Research Square

Preprints are preliminary reports that have not undergone peer review.
They should not be considered conclusive, used to inform clinical practice,
or referenced by the media as validated information.

THz Calorimetry of Electrolyte Solutions Links Water's H-Bond Network to Macroscopic Properties

Gerhard Schwaab

gerhard.schwaab@rub.de

Ruhr-Universität Bochum https://orcid.org/0000-0003-2136-907X

Chun Ma

Physikalisch-Technische Bundesanstalt https://orcid.org/0009-0009-5096-1364

Simone Pezzotti

ENS, PSL, CNRS https://orcid.org/0000-0003-2023-3648

Martina Havenith

Ruhr-Universität Bochum https://orcid.org/0000-0001-8475-5037

Article

Keywords:

Posted Date: November 9th, 2026

DOI: https://doi.org/10.21203/rs.3.rs-11463600/v1

License: This work is licensed under a Creative Commons Attribution 4.0 International License.
Read Full License

Additional Declarations: There is **NO** Competing Interest.

THz Calorimetry of Electrolyte Solutions Links Water's H-Bond Network to Macroscopic Properties

Chun Yu Ma[1,2], Simone Pezzotti[1,3], Martina Havenith[1*], Gerhard Schwaab[1*]

[1*]Physical Chemistry II, Ruhr University Bochum, Universitaetsstrasse 150, 44780, Bochum, Germany.
[2]Unit of Length, Physikalisch-Technische Bundesanstalt, Bundesallee 100, Braunschweig, 38116, Germany.
[3]Laboratoire CPCV, Department de Chimie, Ecole Normale Superieure, PSL University, Sorbonne University, CNRS, France.

*Corresponding author(s). E-mail(s): martina.havenith@rub.de; gerhard.schwaab@rub.de;
Contributing authors: chun.ma@ptb.de; simone.pezzotti@ens.psl.eu;

Abstract

Understanding the macroscopic properties of aqueous electrolyte solutions over their full solubility range requires a detailed microscopic picture of water-ion interactions. We combine THz calorimetry and dimensionality-reduction techniques to demonstrate that two to four spectroscopic markers are sufficient to describe ion-specific variations in mixing entropies and enthalpies, viscosity, and limiting conductivity across 19 electrolytes. Those markers allow us to classify electrolytes as 'strong' or 'weak' and report on changes in the water's H-bond network. As concentration increases, spectroscopic nonlinearities due to ion aggregation appear that, based on a multipole expansion model for activities, are correlated with density changes. For CsI and LiCl, as prototypes of weak and strong electrolytes, respectively, the multipole expansion model accurately describes their conductivities, viscosities, and surface tensions. THz spectroscopy in combination with an activity coefficient model directly correlates macroscopic

solution properties with changes in the H-bond network, paving the way towards efficient machine-learning approaches.

Ions in aqueous solution are pivotal for a wide range of scientific questions and technical applications. The local solvent shell structure and dynamics of ions determine the function of ion-selective channels and pumps in organelles, [1] and artificial membranes[2–4] used for desalination, energy storage, and conversion. Rechargeable batteries based on aqueous electrolytes are considered more environmentally friendly than existing Li-ion technologies.[5–9] Charge carriers such as Mg, Na, Zn, or Ca could serve as cost-efficient replacements for Li.[10–12]

Aqueous electrolyte solutions can stabilize ('salt in') or crystallize ('salt out') proteins as described by the Hofmeister effect.[13]. These properties steer aggregation behavior in pharmaceutical formulations,[14] crystallization, liquid-liquid phase separation, and gelification.[15] The classification of an individual anion species within the traditional 'structure maker' and 'structure breaker' framework is oversimplified, as its impact on the H-bond network depends on a subtle balance between weakening hydrogen bonds and increasing their concentration.[16]

Quantitatively predicting activity coefficients of highly concentrated electrolyte solutions is still challenging.[17] While a simple Debye-Hückel approach yields a screening length decaying exponentially and decreasing with concentration, first-principles studies find different decay lengths.[18] Molecular dynamics simulations and experiments suggest that the correlation length in concentrated electrolyte solutions is much larger than predicted by the Debye length.[19] At high concentrations, combined X-ray and simulation studies reveal the presence of ion aggregates.[20–22] These examples illustrate the need to improve our microscopic picture of electrolyte solutions over their full concentration range.

Here, we aim to link microscopic solvation patterns, as probed by terahertz (THz) spectroscopy in the frequency range 1-20 THz (30-640 cm^{-1}), to macroscopic properties of electrolyte solutions. This is a generalization of our earlier work on alcohols,[23–25], small cosolutes,[26–28], and biomolecules[29, 30] towards electrolytes. THz spectroscopy is especially sensitive to ionic rattling motions[31] and to changes in the hydrogen-bond network. A weakening of water-water H-bonds leads to a red-shift of the well-known translational peak at 200 cm^{-1} while the librational region (400-1000 cm^{-1}) is most sensitive to the angular potential-energy surface experienced by the molecules.

1 Results and Discussion

1.1 Separating THz-Spectra at Infinite Dilution and Ion Pairing Effects

We have measured the concentration dependence of the absorption coefficients of 19 electrolytes in water (3.1). These have been converted to effective molar extinction coefficients, $\epsilon^{\text{eff}}(x_B)$, by subtracting the mol fraction weighted molar extinction coefficient of bulk water from the average molar extinction coefficient of the solution (see Figure 1A and S1.2). Macroscopic effective solution properties are defined similarly, allowing them to be directly compared. At low concentrations, $\epsilon^{\text{eff}}(x_B)$ is sufficiently described by a linear term corresponding to the situation at infinite dilution. With increasing electrolyte concentration, ion association leads to nonlinearities.

$$\epsilon^{\text{eff}} = x_B \left[\epsilon^{\infty} + \epsilon_{\text{nl}}\left(x_B\right)\right] \tag{1}$$

This is similar to what is observed for other thermodynamic functions (see 3.3), such as the effective molar volume, $\bar{\phi}_V^{\text{eff}}$, where the nonlinearity is directly related to the pressure derivative of the difference between activity coefficient, $\ln \gamma_{\pm}$, and osmotic

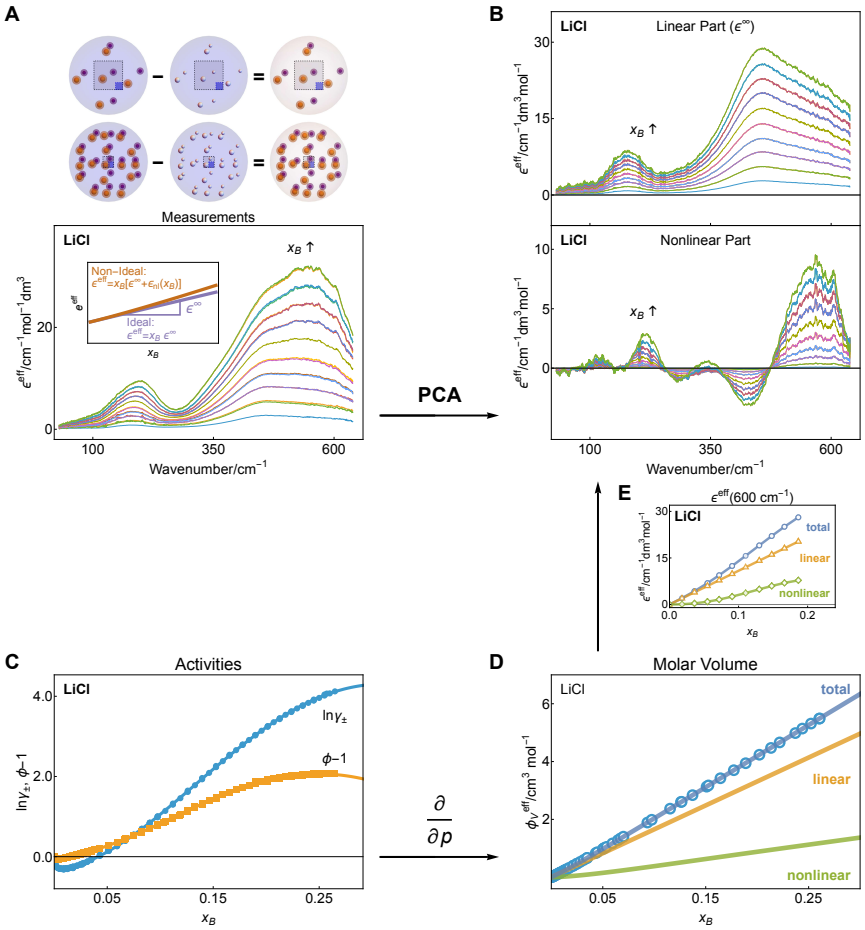


Fig. 1 Single-aqueous-electrolyte data analysis of LiCl. A) The mol fraction weighted water absorption is subtracted from the full absorption spectrum. Normalization by the amount of substance per unit volume (shaded squares) yields the effective ionic absorption coefficient, $\epsilon^{\rm eff}$, which increases with concentration. At higher concentrations, $\epsilon^{\rm eff}$ shows nonlinearities, indicating non-ideal behavior due to the onset of ion aggregation (see inset). B) The concentration-dependent molar extinction coefficients are separated into a linear part (top) and a nonlinear part (bottom) corresponding to the spectra at infinite dilution and ion aggregation, respectively, using principal component analysis (PCA) as a dimension reduction method. C) To describe the nonlinearities, we use a top-down approach starting with the excess thermodynamics, which is determined by the electrolyte activity, $\ln\gamma_\pm$, and water's osmotic coefficient, ϕ. D) Recently, [32], we developed an activity coefficient model that allows us to express the molar volume, $V_m = \partial G_m/\partial p$, as a combination of a linear term and the pressure derivative of the model parameters. As an example, we show the effective molar volume of LiCl and its decomposition into linear and nonlinear contributions; see the text for details. E) The same approach can be applied to model the spectroscopic nonlinearities. This allows us to analyze the physical correlation between the non-idealities of different macroscopic properties.

coefficient, ϕ (see Figure 2C and D):

$$\bar{\phi}_V^{\text{eff}} = x_B \left[\phi_V^{\infty} + \phi_V^{nl}\right] = x_B \left[\phi_V^{\infty} + \nu RT \left(\frac{\partial(\ln \gamma_{\pm} - \phi)}{\partial p}\right)\right]. \tag{2}$$

$\nu = \nu_+ + \nu_-$ is the total stoichiometric factor of the electrolyte while R and T are the universal gas constant and the temperature, respectively.

This allows us to leverage our generalized multipole expansion model[32] (Figure 1C). It allows for efficient description of activity coefficients over the full concentration range (see 1.3.1, Table S1 for definitions, and Figure S2). With its adaptive coarse-grained approach, it yields an expression that is Gibbs-Duhem integrable, so that the same set of parameters determines both electrolyte and water activities. The number of parameters depends on the electrolyte and ranges from two for CsI to seven for LiCl. Thus, the nonlinearity in the effective molar volume is determined by the pressure dependence of the parameters that describe the activities of the electrolyte and water. We find that, typically, two derivatives are necessary to model $\bar{\phi}_V^{\text{eff}}$ and the density (S1.3). Although this analysis is based on a very different set of nonlinear functions, ϕ_V^{∞} agrees well with literature data (Figure 6).

Starting from the hypothesis that the nonlinearities of ϵ^{eff} have a similar origin as those of $\bar{\phi}_V^{\text{eff}}$, we used the same approach to separate spectroscopic linear and nonlinear concentration dependencies (Figure 1E). To identify the relevant spectroscopic contributions and their concentration dependence, we employed principal component analysis (PCA,3.4).PCA is especially suited since it allows us to separate features common to all electrolyte spectra from those relevant for individual ions (Figure 2A). A single-parameter derivative suffices to describe the nonlinear, concentration-dependent spectral contributions. LiCl requires an additional derivative. Here, we observe a strong nonlinear contribution indicating a blueshift in one of LiCl's librational bands upon ion aggregation (Figure 2B). Data for all electrolytes are shown in S1.4.

1.2 THz-based Classification of Electrolytes: Energetics and Transport Processes

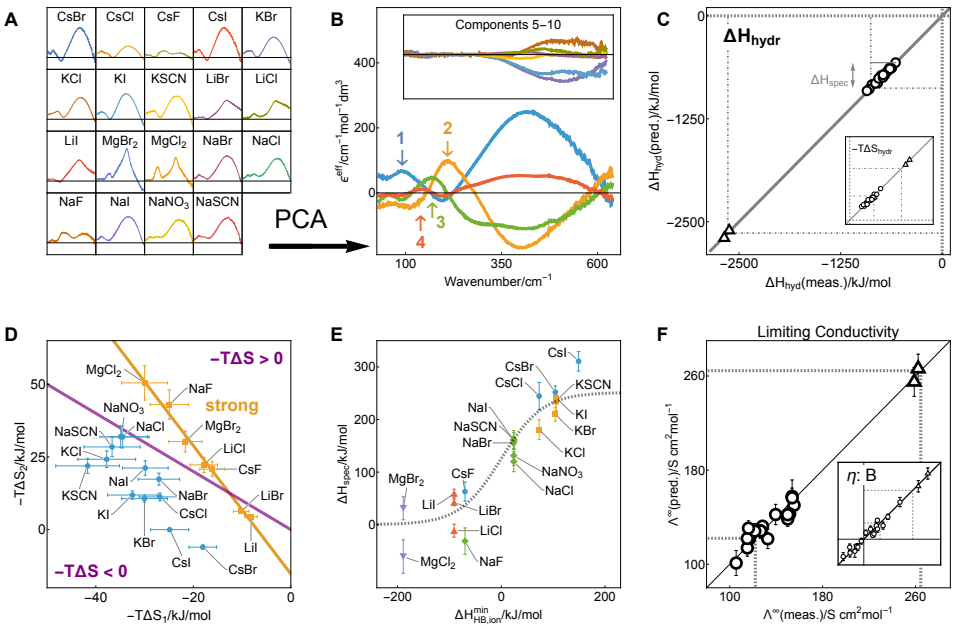


Fig. 2 Combined analysis of spectra at infinite dilution. A) We separate the spectra of 19 electrolytes at infinite dilution into B) H-bond-network (1-4) and ion-related (5-10, inset) spectroscopic components using principal component analysis. C) The information from two and four THz spectroscopic markers suffices to describe the ion-specific hydration entropy (inset) and enthalpy (ΔH_{spec}), respectively, at infinite dilution beyond purely electrostatic terms (thin dashed lines for monovalent, circles, and divalent, triangles, salts, respectively). The spectroscopically derived entropic and enthalpic terms span a high-dimensional space that can be projected to obtain different unbiased electrolyte classifications: D) Projection into the entropy contributions from 2^{nd} vs 1^{st} spectral component (The purple line separates regions of posietive and negative energetic contributions) E) Projection into the ΔH_{spec} and $\Delta H_{\mathrm{HB,ion}}$ components, as defined in the text, showing a sigmoidal behavior. F) Linear models that are based on the THz spectroscopic markers are also able to describe quantitatively dynamic solution properties at infinite dilution, such as viscosity (inset) and conductivity. This is shown by the strong correlation between the linear models and the literature data.

1.2.1 Extracting THz Spectroscopic Markers

We first focus on the linear spectral components and their connection to ion-specific mixing energies at infinite dilution. To separate water-specific and ion-related signatures, we applied PCA in two steps: First, we focused on the translational part of the

spectrum, which is very sensitive to local hydrogen-bond properties: We investigated a subset of 14 electrolytes in the frequency range 30-250 cm^{-1}, see Figure 7, which covers the intermolecular H-bond stretching mode of water, which is observed at 220 cm^{-1} in ice, shifts to 209 cm^{-1} in clathrates[33] and to 190 cm^{-1} in room-temperature water and to 130-170 cm−1 for water at extended interfaces and around small solutes.[27, 28, 31] Additional water modes are centered between 80 and 300 cm^{-1} in bulk water.[34] Electrolytes containing Li^{+} and Mg^{2+} were not considered in this step.

Second, we applied a PCA for all 19 electrolytes over the spectroscopic region 30-640 cm^{-1}, Figure 2B (see 3.4 and Figure 8 or details). Ten principal components ($C_1 - C_{10}$) describe the spectra of 19 electrolytes with 11 distinct ions. This suggests that some of the PCs describe ion-independent properties. To preserve information from the low-frequency analysis, we rotated the PCs from the full-frequency onto those of the low-frequency analysis. Of the ten components, four are relevant for the connection to thermodynamic and macroscopic properties.

C_2 shows a strong band at 210 cm^{-1} as well as a steep slope from 400-600 cm^{-1}. We can compare this to the H-bond stretch-mode of clathrates at 210 cm^{-1}[33] and to the spectroscopic signature of 'bound water', i.e., to the steep slope ($\delta\alpha/\delta\nu$) between 400 and 600 cm^{-1} of the water population H-bonded to the OH-group around alcohols.[25] C_3 peaks at 170 cm^{-1}, characteristic of red-shifted or weaker intermolecular interaction.[25] C_4 peaks at 140 cm^{-1} and shows a positive contribution in the librational region above 250 cm^{-1}. Both observations indicate a further weakening of the contributing H-bonds. All higher principal components make negligible contributions to the translational frequency range.

By construction, C_1 is the CsI spectrum, since CsI has the smallest hydration free energy of all electrolytes investigated.[35] Summarizing our analysis, we have identified four spectroscopic markers that span a wide range of H-bond motifs and are expected to be closely related to ion-specific solution properties.

1.2.2 Classification of Electrolytes

To connect THz spectroscopic data to hydration properties, we employed Marcus's collection of macroscopic thermodynamic data at infinite dilution,[35] i.e., absolute hydration enthalpies, entropies, and Gibbs free energies for the transfer of the individual ions from the gas phase into the solution. We converted these data to electrolyte properties, assuming additivity of single-ion properties. This additivity is preserved in our analysis below.

Table 1 Fit parameters at infinite dilution as obtained from a global fit of ΔH_{hyd}, ΔS_{hyd} and ΔG_{hyd}. For completeness, we added the fit results for the Jones-Dole B coefficient and the limiting conductivity, Λ^{∞} (see Figure 2F). The number in brackets corresponds to the errors in units of the last digit.

Component	a	b	PC 1	PC2	PC 3	PC4
ΔH_{hyd} (kJ/mol)	-440(3)	-	311(9)	-313(13)	-78(11)	-78(12)
$-T\Delta S_{\mathrm{hyd}}$ (kJ/mol)	13(1)	16(2)	-25(2)	43(3)	-	-
B (dm^3/mol)	0.0048(5)	-	-0.2(1)	0.31(2)	-	0.06(2)
Λ^{∞} (S cm^2/mol)	27(3)	34(5)	35(6)	-51(8)	-	-20(7)

The spectroscopic information contained in the linearly concentration-dependent components was mapped into this set of infinite dilution thermodynamic quantities via a global fit over all electrolytes, applying the following linear model:

$$\Delta E_i = \Delta E_{\mathrm{a}} \sum_j \nu_{ij} q_{ij}^2 + \Delta E_{\mathrm{b}} \sum_j \nu_{ij} + \sum_{k=1}^{n} \Delta E_k \tilde{s}_{ik} \tag{3}$$

where ΔE can be enthalpy, ΔH_{hyd} or entropy, $-T\Delta S_{\mathrm{hyd}}$. The first two terms depend on the stoichiometry of the electrolyte and are not ion specific: ν_{ij} is the stoichiometric coefficient, q_{ij} the charge of each ion, and the index, j, runs over cation and anion. ΔE_{a} and ΔE_{b} are fitting parameters that are the same for all electrolytes. The third term contains the ion-specific contributions which are determined solely by spectroscopic

information. The set of $\{\tilde{s}_{ik}\}$ is the scores as obtained from our PCA analysis for electrolyte i, and ΔE_k is the energetic contribution attributed to the THz spectroscopic marker, k. In the final fit (see Methods for details), we used the combination of ΔH_{hyd}, $-T\Delta S_{\mathrm{hyd}}$, and the Gibbs free energy, $\Delta G_{\mathrm{hyd}} = \Delta H_{\mathrm{hyd}} - T\Delta S_{\mathrm{hyd}}$, to obtain a set of global fit parameters (see Table 1). Figure 2C shows that four(two) spectroscopic markers suffice to reproduce ion-specific variations of hydration enthalpy(entropy, see inset, Gibbs energy see Figure 9). This establishes a direct spectroscopy-thermodynamic mapping for the dilute regime. Equation 3 allows us to separate electrostatic (ΔE_{a}, ΔE_{b}) and ion-specific (ΔE_k) energetic contributions (see ΔH_{spec} in Figure 2C) using THz spectroscopy.

The spectroscopically derived free-energy terms span a high-dimensional space that can be projected to obtain different unbiased electrolyte classifications. A particularly interesting projection is shown in Figure 2D where the two dominant principal components fully determine the entropic contribution. The purple line separates negative (lower-left) from positive (upper-right) regions. When plotting the entropy derived from C_2 versus that obtained from C_1, two groups of electrolytes can be clearly distinguished: 'Strong' Electrolytes containing at least one ion interacting strongly with water (Yellow: LiI, LiBr, LiCl, NaF, CsF, $MgBr_2$, $MgCl_2$) show a linear relationship with a negative slope. These electrolytes lie mostly in the entropically unfavorable region. Electrolytes without a strong ion (in blue) are in the entropically favorable region. The entropic gain increases with distance from the purple line, i.e., qualitatively with increasing ion radius and decreasing ion-water interaction. NaCl and $NaNO_3$ are close to this line and can be considered "entropically neutral".

This picture is supported by Figure 2E where we investigate how ΔH_{spec} depends on the ion-water interaction strength $\Delta H_{\mathrm{HB,ion}} = \Delta H^{\mathrm{ion}}_{\mathrm{hyd}} - q^2_{\mathrm{ion}}\Delta H_a$ of ions after subtraction of a Born-like contribution that only depends on the ion charge. We find that H_{spec} is dominated by $H^{\mathrm{min}}_{\mathrm{HB,ion}}$, i.e., by the ion that is more strongly interacting with

water, independent of its nature as an anion or cation. All electrolytes labeled 'strong' above contain ions that show negative $\Delta H_{\mathrm{HB,ion}}$ and possess a long-lived hydration shell with a fixed number of water molecules.[36, 37] The interaction between the second-shell and first-shell water leads to their low-intensity THz response. The distribution shows sigmoidal behavior: ΔH_{spec} increases as ion-water interaction strength decreases. The ion that interacts most strongly with water dominates the spectroscopically derived enthalpy contribution. The counter-ion water interaction modulates this effect such that at constant $\Delta H^{\mathrm{min}}_{\mathrm{HB,ion}}$, ΔH_{spec} increases with decreasing counterion-water interaction. The PCA allows us to separate H-bond-related and ion-specific contributions to ϵ^{∞} (Figure S9). Our THz-based approach also describes macroscopic transport properties (limiting conductivity: Figure 2F, Jones-Dole B-coefficient: see inset and Methods for details).

1.3 How Does the H-bond Network Contribute to the Energetics of Ion Aggregation?

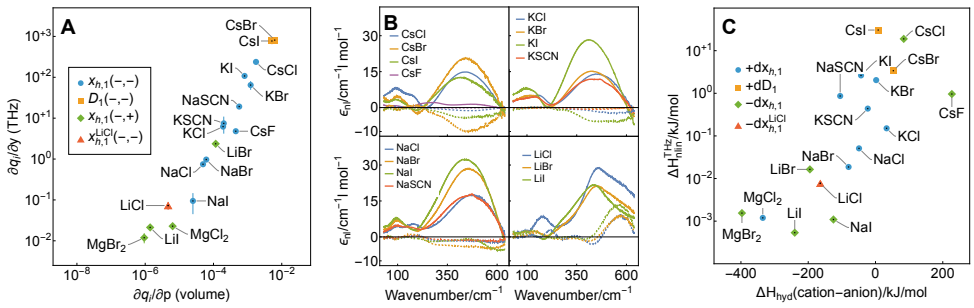


Fig. 3 Analysis of the nonideal spectroscopic partial contributions. A) We have plotted here a comparison between the deduced nonlinear component in the experimentally observed THz spectra with the derivative of the molar volume change, and observe a clear correlation. The signs in brackets correspond to density and spectroscopic changes, respectively. B) Linear and nonlinear contributions of the measured electrolytes at the highest concentration, displayed for distinct cations. C) Spectroscopically determined nonlinear enthalpic contribution of the electrolytes as a function of hydration enthalpy difference between anion and cation.

1.3.1 A Thermodynamic Toolbox to Describe Ion Aggregation

When comparing the nonlinearities in ϵ^{eff} and $\bar{\phi}_V^{\text{eff}}$, we find that the spectroscopic nonlinearity is strongly correlated to a subset of the nonlinear density changes (Figures 3A and discussion below). This encouraged us to employ the multipole expansion model,[32] that we recently introduced to connect macroscopic and spectroscopic properties.In a nutshell, our model describes the interaction between a spherical central observation volume and the excess charge distribution arising from both ions and water in the surrounding layers. For each concentration, the central observation volume is adaptively chosen to contain a single electrolyte unit and the corresponding stoichiometric amount of water. This interaction can be written as a multipole expansion of the electric field generated by the ions and water in the observation volume, with the excess charge distribution due to solute and solvent in each layer outside the observation volume. Integrating over all layers yields the logarithm of the electrolyte's activity coefficient:

$$\ln \gamma_{\pm}(x_B) = \sum_{l=1}^{l_{\max}\leq 3} D_l \left(\frac{x_B}{x_h^l}\right)^{\lambda_l} \ln\left[\left(\frac{x_B}{x_h^l}\right)^{\lambda_l}\right] \tag{4}$$

where l=1, 2, 3 correspond to the dipolar, quadrupolar, and octupolar expansion terms, respectively.

In this picture, $\ln \gamma_{\pm}$ and ϕ contain contributions from both solute and solvent charge distributions. Over an extensive set of 138 electrolytes, at maximum, a third-order expansion is sufficient to describe the electrolyte activity up to the solubility limit. For many electrolytes, a purely dipolar description is sufficient. The quadrupole and octupole expansion terms describe short-range interactions, as expected for ion aggregation. Each parameter has a clear physical meaning: x_h^l is a crossover mol fraction from dipolar to complex ion interaction and characterizes the transition from exergonic ($x < x_h^l$) to endergonic ($x > x_h^l$) dipolar interaction energy so that

$\ln \gamma_{\pm}^{(l)}(x_h^l) = 0$. For the quadrupole and octupole terms, $x_h^2 = x_h^3 = 1$. D_l describes the interaction strength of the observation volume with all surrounding ions. For the interaction between the central observation volume and the surrounding interacting shells, we observe a power-law behavior of the form $\delta D_l(n_D) \propto 1/n_D^{1+3\lambda_l}$ as the distance, n_D, from the central volume increases. The parameter, λ_l, determines the effective interaction coefficient. Larger values of λ correspond to shorter-range interactions.

The model's major advantage is the Gibbs-Duhem integrability of each expansion term, yielding an analytical expression for the corresponding osmotic coefficient. This allows us to derive the full set of activity coefficients from measurements of any combination of electrolyte activity, osmotic coefficient, and water activity (see Figure 1C). Its particular strength becomes fully apparent when considering derived excess thermodynamic variables, such as the volume $V = (\partial G/\partial p)_T$ in terms of the Gibbs energy G. Since $\ln \gamma_{\pm}$ and ϕ depend on the same set of parameters, Equation 2 can be rewritten as

$$\bar{\phi}_V^{\text{eff}} = x_B \left[\phi_V^{\infty} + \nu RT \sum_i \left(\frac{\partial \left(\ln \gamma_{\pm} - \phi \right)}{\partial q_i} \right) \frac{\partial q_i}{\partial p} \right] \tag{5}$$

where $\{q_i\}$ is the set of two to seven parameters describing the activity coefficients of solute and solvent, and $\frac{\partial q_i}{\partial p}$ are their pressure derivatives.

1.3.2 Mapping Spectroscopy to Nonlinear Density Changes

We used Equation 5 to fit the effective apparent molar volume derived from density measurements [38]. The effective molar volumes and densities are well reproduced by Equation 5 (see Figures S8 and S4). The apparent molar volumes at infinite dilution agree nicely with those reported in the literature (see Figure 6).[39] In most cases (see Figure 3A), the pressure derivatives of two dipolar interaction parameters, i.e., interaction strength, D_1, and the crossover mol fraction, x_h^1, contribute to the nonlinearity of $\bar{\phi}_V^{\text{eff}}$. Exceptions are CsI, where D_1 suffices, and LiCl, which requires including the quadrupolar interaction strength, D_2.

While molar volume nonlinearities typically require two parameter derivatives, we are able to describe the nonlinearity observed in the concentration dependence of the THz spectra by a single parameter derivative (see Equation 5). Figure 3A shows that their absolute amplitudes strongly correlate. This indicates that THz-spectroscopic nonlinearities are closely related to density changes but cannot fully account for them. The performed mapping establishes a quantitative connection between the nonlinearities in spectroscopic, thermodynamic, and density properties of concentrated electrolyte solutions, up to the solubility limit.

1.3.3 The H-bond Contribution to Ion-Pair Energetics

In section 1.2, we introduced four THz spectroscopic markers that enable us to energetically classify 19 electrolytes containing 11 ionic species at infinite dilution. The markers show signatures in the translational (80 to 250 cm^{-1}) and librational (300 to 640 cm^{-1}) frequency regions that indicate hydrogen bonds from very strong (C_2), intermediate (C_3, C_4) to very weak (C_1, i.e. CsI). This indicates that they are directly related to the partial contribution, which is common for all electrolytes, i.e., the solvent water and its H-bond network. Combined with the strong correlation between molar volume and spectroscopic changes, this provides an opportunity to quantify the energetic contribution of the H-bond network to ion pairing and to ion-specific counterion effects.

Ion pairing is expected to distort the H-bond network and, therefore, shift the relative weights of the four H-bond populations identified spectroscopically. Since we know the spectral characteristics of the nonlinear changes for the different electrolytes and how different H-bond motifs can be converted into energetic contributions, we can derive the nonlinear THz mixing enthalpy, $\Delta H_{\mathrm{nlin}}^{\mathrm{THz}}$, which describes the energetic contribution of the H-bond network to the total mixing energetics upon ion pair formation.

$\Delta H_{\mathrm{nlin}}^{\mathrm{THz}}$ is determined by projecting the nonlinear spectra onto the principal components derived in 1.2.2 and converting the spectroscopic weights into ion-pair-specific energetic contributions (see Methods for details).

Figure 3B shows a comparison of the linear and nonlinear spectroscopic contributions at the highest measured concentration for different electrolytes sorted by cation, since the cation dominates the overall shape of the nonlinearity (see SI for a full dissection and Figure S8). This is supported by Figure 3C, where we show $\Delta H_{\mathrm{nlin}}^{\mathrm{THz}}$ as a function of the difference between cationic and anionic hydration enthalpy, ΔH_{hyd}(cation-anion). Figure 3C indicates a clear correlation between $\Delta H_{\mathrm{nlin}}^{\mathrm{THz}}$, and the ion-water interaction strength: Electrolytes containing cations with strong ion-water interaction ($H_{\mathrm{hydr}}^{\mathrm{cat}} \ll 0$) and, therefore, a large negative difference between cationic and anionic hydration enthalpy show a $\Delta H_{\mathrm{nlin}}^{\mathrm{THz}}$ which is three to four orders of magnitude smaller compared to those of electrolytes with a weak ion-water interaction and positive ΔH_{hyd}(cation-anion). The relationship also holds for CsF, with F^- as the anion, which strongly interacts with water. This contrasts with our finding at infinite dilution (see Figure 2E), where the strongest water-ion interaction dominates the spectroscopically derived enthalpy, independent of ion charge.

2 Conclusions

Summarizing our analysis, we have shown that a top-down approach, based on a generalized multipole expansion model for electrolyte and water activities,[32] can decompose excess molar volumes and molar extinction coefficients into their infinite-dilution and ion-aggregation components. This allows us to correlate spectroscopic, molecular, and macroscopic properties of electrolyte solutions within a unified framework. To test whether this approach applies to other macroscopic properties, we used LiCl and CsI as the extreme cases of strong and weak electrolytes. Literature

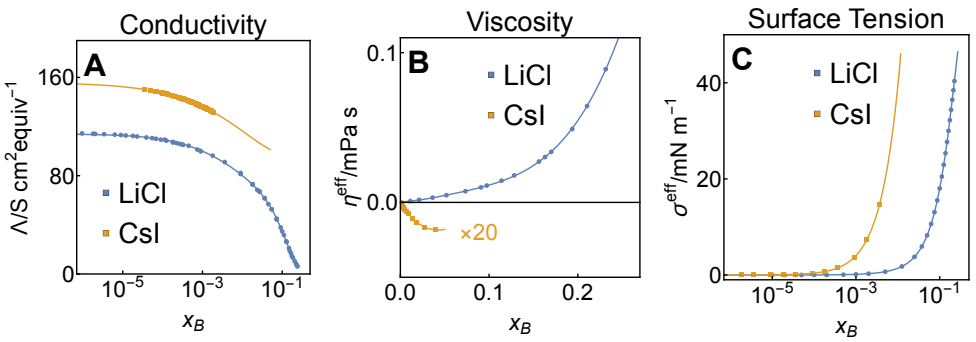


Fig. 4 Relation between the activity coefficient model and macroscopic solution properties. A-C) Parameter derivatives of the multipole expansion model (see text for details) allow for the description of macroscopic solution parameters, such as conductivity, viscosity, and surface tension.

data for conductivity,[38], viscosity,[38], and surface tension at 25°C[40, 41] were converted to effective values prior to modeling their concentration dependencies based on adapted versions of Equation 5 (see SI for details). Figures 4A-C show that the corresponding fits agree well with experimental data over the full concentration range. All nonlinearities show a consistent pattern: dipolar parameter derivatives dominate the nonlinearity. As a perspective, this is an ideal situation for a Bayesian Machine-Learning approach: Each macroscopic property contains information on parameter derivatives and on a subset of the parameters determining the activity coefficients. A comparison of the interdependencies among these parameters provides important benchmarks for simulations. It opens the door to a bottom-up approach to determining electrolyte and water activity using a minimal set of precise measurements.

3 Methods

3.1 Experimental

We investigated in this work a total of 19 electrolytes formed by monovalent cations (Li^+, Na^+, K^+ and Cs^+), monovalent anions (F^-, Cl^-, Br^-, I^-, SCN^- and NO_3^-) and Mg^{2+}. Dry NaCl, KCl, KBr, and CsBr were purchased from Carl Roth GmbH + Co.

KG (Germany), VWR Chemical Co. Ltd (USA), Honeywell Lab Chemicals (Thermo Fisher Scientific, USA), and Alfa Aesar (Thermo Fisher GmbH, Germany), respectively. Other chemicals were purchased from Sigma-Aldrich Corporation (St. Louis, MO, USA). All samples have purities of over 99.5% and aqueous electrolytes were prepared by dissolving the salts in ultrapure water without further purification. To prevent degradation due to oxygen and light, electrolytes including LiBr, LiI, NaSCN, and KSCN were prepared in a glove box with controlled illumination. Table 2 shows the 19 electrolytes under investigation. Broadband THz/FIR transmission spectra of the aqueous solutions were measured at 20°C with a spectral frequency range of 30 to 640 cm^{-1} and a spectral resolution of 1 cm^{-1}. The sample was placed in a measurement cell between two diamond windows, separated by a Kapton spacer with a typical thickness of 13 μm. The sample thickness was independently determined in the mid-infrared region by measuring the interference pattern of the empty cell. The densities of the solutions were measured with a density meter (Anton Paar GmbH, DMA 58) at 20°C to determine precise molarity.

Table 2 Investigated electrolytes in this work.

Li^+	Na^+	K^+	Cs^+	Mg^{2+}
	NaF		CsF	
LiCl	NaCl	KCl	CsCl	$MgCl_2$
LiBr	NaBr	KBr	CsBr	$MgBr_2$
LiI	NaI	KI	CsI	
	NaSCN	KSCN		
	$NaNO_3$			

Using Lambert-Beer's law, the frequency-dependent absorption coefficient of an aqueous solution ($\alpha_{sol}(\nu)$) is expressed as:

$$\alpha_{\mathrm{sol}}(\nu) = \frac{1}{d} \ln \left(\frac{I_{\mathrm{bulk}}(\nu)}{I_{\mathrm{sol}}(\nu)} \right) + \alpha_{\mathrm{bulk}}(\nu) \tag{6}$$

where d is the sample thickness, $I_{\mathrm{bulk}}(\nu)$ and $I_{\mathrm{sol}}(\nu)$ are the transmitted intensities of the water reference and the sample, respectively, and $\alpha_{\mathrm{bulk}}(\nu)$ is the absorption coefficient of water at the temperature of 20°C. To obtain $\alpha_{\mathrm{bulk}}(\nu)$, we fitted the complex molar susceptibility of water as a superposition of damped harmonic oscillator functions and calculated the absorption coefficient using the equations given by Zelsmann.[42] The data included in the fit were a selection of literature data[43–45] combined with our own measurements. Because all electrolyte solution measurements are referenced to bulk water, and assuming that the change in the THz index of refraction of the salt solution is small compared to that of bulk water, etalon effects that could be mistaken for ionic absorption lines are minimized.

To be able to relate the experimental spectra to thermodynamic quantities directly, we switch to mol fraction units and convert the absorption coefficient into the average molar extinction coefficient:

$$\overline{\epsilon}_{\mathrm{sol}} = \frac{\alpha_{\mathrm{sol}}(\nu)}{c_{\mathrm{B}} + c_w}. \tag{7}$$

c_{B} and c_w are the molarities of the electrolyte and water, respectively, as obtained from density measurements. In a final step, we subtract the bulk water contribution and obtain the effective molar extinction coefficient of the solution:

$$\epsilon^{\mathrm{eff}} = \overline{\epsilon}_{\mathrm{sol}} - (1 - x_B)\epsilon_{\mathrm{bulk}}. \tag{8}$$

Here, x_B is the electrolyte mol fraction and ϵ_{bulk} the molar extinction coefficient of bulk water at the given temperature. This procedure enables us to remove nonlinearities arising from solute concentration-dependent changes in the apparent molar volumes of the solvent and the solute. The observed concentration dependency increases approximately linearly.

3.2 Converting Molality to Mol Fraction Scale

Although molality, molarity, and weight-percent are well-known descriptors for the composition of binary solutions, we have chosen the electrolyte mol fraction, x_B. The main reasons are that the multipole expansion model[32] shows its simplest form in this unit system and is valid over the full mol fraction range $0 \leq x_b \leq 1$, i.e., also in the super-saturated regime. Second, the mol fraction x_B, pressure p, and absolute temperature T provide a set of independent variables to describe thermodynamic functions. We, therefore, show here how molar Gibbs energies in the molality scale can be converted to the mol fraction scale such that the resulting expression matches the one that is valid over the full mol fraction range.

According to Stokes[46] the Gibbs free energy, G as function of electrolyte molality, m_B can be described by

$$\begin{aligned} G &= n_0 \left(\mu_w^0 + RT \ln a_w\right) \\ &+ m_B \left(\mu_s^\infty + \nu RT \left[\ln\left(\left(\nu_+^{\nu_+}\nu_-^{\nu_-}\right)^{1/\nu} \frac{m_B}{m^0}\right) + \ln\gamma_\pm\right]\right) \end{aligned} \tag{9}$$

where $n_0 = 1000\ \mathrm{g}/M_w$ is the amount of water in 1 kg of the liquid, and M_w, μ_w^0, and a_w are the molar mass of water in g/L, the chemical potential of bulk water, and the water activity, respectively. μ_s^∞ is the chemical potential at infinite dilution. We assume that the electrolyte is composed of ν_+ cations and ν_- anions with the total stoichiometric coefficient $\nu = \nu_+ + \nu_-$ leading to the average ionic molality $m_\pm = (\nu_+^{\nu^+}\nu_-^{\nu_-})^{\frac{1}{\nu}} m_B$. For water, we use the bulk liquid as the reference state. The electrolyte is referenced to a hypothetical ideal 1 molal solution (m^0) with no ion-ion interaction, and $\gamma_\pm$ approaches unity for infinite dilution. The water activity, a_w, is related to the osmotic coefficient, ϕ by

$$\ln a_w = -\nu \frac{m_B}{n_0}\phi = -\nu \frac{x_B}{x_w}\phi \tag{10}$$

where n_0 is the amount of water in molar units in 1 kg of the liquid and x_w is the water mol fraction.

Combining Equations 9 and 10 leads to

$$G = n_0\mu_w^0 + m_B\left(\mu_s^\infty + \nu RT\left[\ln\left(\left(\nu_+^{\nu_+}\nu_-^{\nu_-}\right)^{1/\nu}\frac{m_B}{m^0}\right) + \ln\gamma_\pm - \phi\right]\right) \tag{11}$$

To convert Equation 11 to mol fraction units, we show that $\ln(m_B/m^0)$ is the low-concentration approximation of

$$\begin{aligned}\ln(x_B) &= \ln\left(\frac{m_B}{m_B+n_0}\right) \\ &= \ln\left(\frac{m_B/m^0}{(m_B+n_0)/m^0}\right) \\ &= \ln\left(\frac{m_B}{m^0}\right) - \ln\left(\frac{m_B+n_0}{m^0}\right) \\ &\approx \ln\left(\frac{m_B}{m^0}\right) - \ln\left(\frac{n_0}{m^0}\right)\end{aligned} \tag{12}$$

for $m_B \ll n_0$. The last term approaches a constant value at low molalities, which is absorbed in μ_s^∞. As expected, $\ln(x_B)$ vanishes in the limit $x_B \to 1$, i.e. $m_B \to \infty$.

Converting the combined Equs.11 and 12 to mol fraction units yields a molar Gibbs energy,

$$G_m = x_w\mu_w^0 + x_B\left(\mu_s^\infty + \nu RT\left[\ln\left(\left(\nu_+^{\nu_+}\nu_-^{\nu_-}\right)^{1/\nu}x_B\right) + \ln\gamma_\pm - \phi\right]\right) \tag{13}$$

Please note that in standard binary solutions, water activity is written as $\ln a_w = \ln x_w + \ln\gamma_w$. Using Eq. 10 yields

$$\phi = -\frac{x_w}{\nu x_B}\left(\ln x_w + \ln\gamma_w\right) \tag{14}$$

which returns the standard expression for excess molar Gibbs energies when inserted in Equation 13.

3.3 Modeling Effective Properties

3.3.1 Average Molar Volume

The average molar volume of the solution is given by

$$\begin{aligned}\bar{\phi}_V &= \left(\frac{\partial G_m}{\partial p}\right)_T \\ &= (1-x_B)\frac{\partial \mu_w^0}{\partial p} + x_B\left(\frac{\partial \mu_s^\infty}{\partial p} + \nu RT\left[\frac{\partial \ln \gamma_\pm}{\partial p} - \frac{\partial \phi}{\partial p}\right]\right) \\ &= (1-x_B)\phi_W^0 + x_B\left[\phi_V^\infty + \nu RT\left(\frac{\partial \ln \gamma_\pm}{\partial p} - \frac{\partial \phi}{\partial p}\right)\right]\end{aligned} \tag{15}$$

where we have introduced the molar volumes of the electrolyte at infinite dilution, $\phi_V^\infty = \frac{\partial \mu_s^\infty}{\partial p}$, and bulk water $\phi_W^0 = \frac{\partial \mu_w^0}{\partial p}$.[39] $\bar{\phi}_V$ can be determined experimentally from density measurements when the amount of substance of solute and solvent is known. When M_B and M_w are the molar masses of electrolyte and water, respectively,

$$\bar{\phi}_V = \frac{x_B M_B + (1-x_B)M_w}{\rho_{\text{sol}}}. \tag{16}$$

We observe that the effective molar volume

$$\begin{aligned}\bar{\phi}_V^{\text{eff}} &= \bar{\phi}_V - (1-x_B)\phi_W^0 \\ &= x_B\left[\phi_V^\infty + \nu RT\left(\frac{\partial \ln \gamma_\pm}{\partial p} - \frac{\partial \phi}{\partial p}\right)\right] \\ &= x_B\left[\phi_V^\infty + \nu RT\sum_i\left(\frac{\partial\left(\ln \gamma_\pm - \phi\right)}{\partial q_i}\right)\frac{\partial q_i}{\partial p}\right]\end{aligned} \tag{17}$$

is linear in ϕ_V^∞ and contains a nonlinear contribution that depends on the difference of the pressure derivatives of the activity coefficient and the osmotic coefficient $\ln \gamma_\pm$ and

ϕ, respectively. In the last step, we have used the multipole expansion model [32] and expressed the pressure dependence in terms of its parameter derivatives. Figures 6, S3, and S4 show that the electrolyte properties at infinite dilution and the changes of effective molar volume and density over the full mixing range are well described by our model.

3.3.2 Viscosity

Equation 17 can, in a similar form, be used to model viscosity:

$$\begin{aligned} \eta^{\text{eff}} &= \eta - (1 - x_B)\eta_W^0 \\ &= x_B \left[\eta^\infty + \nu RT \sum_i \left(\frac{\partial \left(\ln \gamma_\pm - \phi \right)}{\partial q_i} \right) \frac{\partial q_i}{\partial f_s} \right] \end{aligned} \tag{18}$$

where $\frac{\partial q_i}{\partial f_s}$ is the derivative of a model parameter, when a shear force, f_s, is applied. The linear term, η^∞ corresponds to the B coefficient in the empirical equation by Jones and Dole.

3.3.3 Surface Tension

The model for surface tension can also be directly derived from Equation 17:

$$\begin{aligned} \sigma^{\text{eff}} &= \sigma - (1 - x_B)\sigma_W^0 \\ &= x_B \left[\sigma^\infty + \nu RT \sum_i \left(\frac{\partial \left(\ln \gamma_\pm - \phi \right)}{\partial q_i} \right) \frac{\partial q_i}{\partial A} \right] \end{aligned} \tag{19}$$

where $\frac{\partial q_i}{\partial A}$ is the derivative of a model parameter, when the surface, A, is increased.

3.3.4 Conductivity

Since only the electrolyte contributes to conductivity, we used the model approach

$$\Lambda(x_B) = \Lambda^{\infty} + \nu RT \sum_i \left(\frac{\partial \ln \gamma_{\pm}}{\partial q_i} \right) \frac{\partial q_i}{\partial E} \tag{20}$$

where $\frac{\partial q_i}{\partial E}$ is the derivative of the expansion parameters to the local electric field.

3.4 Principal Component Analysis

3.4.1 Basics

We performed principal component analysis using a Singular Value Decomposition (SVD).[47] SVD allows us to separate important (e.g., dependency on concentration or composition) from unimportant information, such as noise or experimental artifacts. When we apply SVD to a dataset $\mathbf{D}$ containing a list of effective molar extinction coefficients as row vectors, it returns three matrices $\mathbf{S}$, $\mathbf{V}$, and $\mathbf{L}$ such that

$$\mathbf{D} = \mathbf{SVL}^T. \tag{21}$$

The orthonormal matrix $\mathbf{L}$ contains the spectral eigenvectors (sometimes named 'loadings') that are required to describe the data as column vectors with decreasing importance. $\mathbf{V}$ is a diagonal matrix containing the singular values, i.e., the relative importance of each loading. Finally, the orthonormal matrix $\mathbf{S}$ contains the scores of the individual measurements as row vectors.

3.4.2 Dissection and Reconstruction of Concentration-Dependent Molar Extinction Coefficients

A simple example is the separation of concentration-dependent measurements, as shown in Figure 5, into their spectroscopically relevant contributions (loadings) and

the concentration dependence as depicted by the corresponding scores. For this application, we have defined the product

$$\mathbf{P} = \mathbf{V}\mathbf{L}^T \tag{22}$$

as a principal component matrix listing the PCs, C_i, as row vectors in decreasing order of importance. In this picture, each column of $\mathbf{S}$ weights the importance of the corresponding principal component as a function of concentration. To separate information from noise, we can reduce the number of principal components, e.g., by setting all diagonal elements in $\mathbf{V}$ below a certain threshold value to zero.

The original input data can be reconstructed from the relevant principal components $C_i(\nu)$ and their concentration dependencies described by the score functions $s_i\left(x_{el}\right)$, by

$$\epsilon^{\text{eff}}\left(x_B, \nu\right) = \sum_{i=1}^{n} s_i\left(x_B\right) C_i(\nu). \tag{23}$$

Please note that the singular value decomposition is a strictly mathematical procedure that orders principal components according to their ability to describe the variance in a given data set. Any physical insight must come from an interpretation of the mol fraction dependencies of the score functions and an analysis of the composition and line shapes of the spectroscopic components.

We find that, while three principal components are required for LiCl, two principal components are sufficient for all other electrolytes shown in Table 2. The scores of the first and by far strongest principal component are primarily linear, while the second (and third) components show a pronounced nonlinearity. To address this observation, we separate the linear and nonlinear contributions using

$$s_i\left(x_B\right) = a_{i0} x_B + \sum_{j=1}^{k} a_{ij} f_j^{\text{nl}}(x_B) \tag{24}$$

where a_{ij} and $f_j^{\mathrm{nl}}(x_B)$ are proportionality factors and nonlinear functions describing the mol fraction dependency of the individual scores, respectively. The nonlinear functions, $f_j^{\mathrm{nl}}(x_B)$, are directly derived from the parameter derivatives of the multipole expansion model (see Equation 5). The usefulness of this approach is demonstrated in Figures S6 and S7, which show the spectra reconstructed using Equs. 23 and 24 and the resulting residuals.

3.4.3 Extracting H-Bond-Related Spectroscopic Markers from Infinite-Dilution Spectra

In this PCA application, we use the molar extinction coefficients at infinite dilution of the investigated electrolytes to determine a set of principal components as described by Equation 22 to reconstruct the original spectra by

$$\epsilon_i^{\infty}(\nu) = \sum_{j=1}^{n} s_i C_j(\nu) \tag{25}$$

where i labels the electrolyte and s_i are its corresponding scores. $C_j(\nu)$ depicts the n principal components that are necessary for the reconstruction of the input spectra.

3.4.4 Advanced PCA: Rotation of Full-Range on Translation Range Principal Components

The PCA can be modified by inserting a rotational matrix, $\mathbf{R}$, and its inverse in Equation 21 such that

$$\mathbf{D} = \left(\mathbf{S}\mathbf{R}^{-1}\right)\left(\mathbf{R}\mathbf{V}\mathbf{L}^{T}\right) = \mathbf{S'P'}. \tag{26}$$

with **S'** and **P'** as rotated score and principal component matrices, respectively. This mathematical operation leaves the reconstruction unchanged while allowing us to modify the dissection based on physical insight.

We used this method to connect the full frequency analysis to thermodynamically relevant spectroscopic signatures. We rotated $\mathbf{P}^{\text{full}}_{LF,10}$, the low-frequency range (30-250 cm^{-1}) of the first ten principal components of the full analysis such that the deviations to $\mathbf{P}^{\text{trans}}_{LF,10}$, the first 10 principal components of the restricted translational data set are minimized (see Figure 2B). The rotation matrix, $\mathbf{R}_{LF}$, is given by

$$\mathbf{P}^{\text{trans}}_{LF,10} = \mathbf{R}_{LF}\mathbf{P}^{\text{full}}_{LF,10} \Longrightarrow \mathbf{R}_{LF} = \mathbf{P}^{\text{trans}}_{LF,10} \cdot \left(\mathbf{P}^{\text{full}}_{LF,10}\right)^{-1} \tag{27}$$

where $\left(\mathbf{P}^{\text{full}}_{LF,10}\right)^{-1}$ represents the pseudoinverse of the rectangular matrix $\mathbf{P}^{\text{full}}_{LF,10}$. The rotated set of relevant PCs for the full data set and their corresponding scores are obtained by

$$\begin{aligned} \mathbf{P'}^{\text{full}}_{10} &= \mathbf{R}_{LF}\mathbf{P}^{\text{full}}_{10} \\ \mathbf{S'}^{\text{full}}_{10} &= \mathbf{S}^{\text{full}}_{10}\,(\mathbf{R}_{LF})^{-1} \end{aligned} \tag{28}$$

and shown in Figure 2B.

3.4.5 Using CsI as a Spectroscopic Reference

It is clearly visible that the first principal component still contains a signature of chloride rattling around 180 cm^{-1}.[31] To remove this chloride contamination, we picked CsI as a reference. The resulting scores are given by

$$\begin{aligned} \tilde{s}_{\text{CsI},1} &= 1 \\ \tilde{s}_{\text{CsI},j} &= 0 \qquad\qquad (2 \leq j \leq 10) \end{aligned} \tag{29}$$

$$
\begin{aligned}
\tilde{s}_{i1} &= \frac{s_{i1}}{s_{\mathrm{CsI},1}} \\
\tilde{s}_{ij} &= s_{ij} - \frac{s_{i1}}{s_{\mathrm{CsI},1}} s_{ij} \qquad (2 \leq j \leq 10) \\
\tilde{s}_{ij} &= s_{ij} \qquad (j > 10)
\end{aligned}
$$

This set of equations transforms the first principal component to the CsI spectrum and leaves the remaining principal components unaffected.

3.5 Model for Hydration Energies

We expect that the total energetics is a combination of long-range Coulombic interactions, entropic costs associated with the formation of cavities to host ions in solution, and short-range distortions of the hydrogen-bond network, as characterized spectroscopically. The long-range Coulombic interactions are taken into account via a Born term

$$
\Delta H_{\mathrm{coul}} \propto \sum_i \nu_i q_i^2 \left(1 - \frac{1}{\epsilon(T)}\right) \tag{30}
$$

with stoichiometric coefficients, ν_i, ion charges, q_i, and $\epsilon(T)$ as dielectric constant of the solvent. (see [48] for details on why this approach is useful). Since ϵ is temperature dependent, it follows that this term will also contribute to the hydration entropy. The entropic costs of entropy formation are considered to be proportional to the number of ions per electrolyte sub-unit (i.e., three for the magnesium salts, two for the 1:1 electrolytes). Thus, for electrolyte i, the total model is of the form

$$
\begin{aligned}
\Delta H^{(i)}_{\mathrm{hyd}} &= \Delta H_{\mathrm{B}} \sum_j \nu_{ij} q_{ij}^2 + \sum_{k=1}^{n} \Delta H_k \tilde{s}_{ik} \\
-T\Delta S^{(i)}_{\mathrm{hyd}} &= -T\Delta S_{\mathrm{B}} \sum_j \nu_{ij} q_{ij}^2 - T\Delta S_{\mathrm{cav}} \sum_j \nu_{ij} - \sum_{k=1}^{n} T\Delta S_k \tilde{s}_{ik} \\
\Delta G^{(i)}_{\mathrm{hyd}} &= \Delta H^{i}_{\mathrm{hyd}} - T\Delta S^{i}_{\mathrm{hyd}}
\end{aligned} \tag{31}
$$

where ν_{ij} and q_{ij} are the stoichiometric coefficients of anions and cations, and their corresponding charges, respectively. The $\tilde{s}_{ik}$ are the scores of the principal components as defined in Equation 29.

Figure 9 shows the result of a weighted global fit of ΔH_{hyd}(A), ΔS_{hyd}(B), and ΔG_{hyd}(C) with respect to the literature data. The fit weights (0.001 for ΔH_{hyd} and ΔG_{hyd}, 0.05 for ΔS_{hyd}) were estimated from the inverse of the variance of fits of the individual electrolyte properties. We found that the first two principal components are sufficient to reproduce the hydration entropy to within experimental uncertainty. In comparison, four principal components are required to accurately describe the hydration enthalpy and Gibbs free energy. The fit parameters are shown in Table 1. Tests showed that reducing the number of principal components dramatically increases the fit uncertainty, whereas increasing it yields no significant improvement.

Supplementary information. Supplementary information for the article contains a table of terms and definitions, figures containing effective molar extinction coefficients, fits of the activity and osmotic coefficients, fits of effective molar volumes and densities, the relevant principal components, fits of the spectroscopic scores, and the spectral reconstruction based on the PCA for all 19 electrolytes, A figure showing the linear and nonlinear contributions and a figure separating the spectra at infinite dilution into H-bond-related and ion-specific contributions

Acknowledgements. This study is funded under Germany´s Excellence Strategy – EXC 2033 – 390677874 – RESOLV and by the European Research Council (ERC, Grant Agreement No. 101077129)

Conflict of interest/Competing interests. Nothing to declare

Data Availability. The data will be made available under the DOI

https://doi.org/10.17877/RESOLV-2026-VQW5PS

Author Contribution. G.S. and M.H. developed the study concept. C.Y.M. performed the measurements, initial data processing, and exploratory data analysis. G.S. performed the advanced data analysis and data curation. G.S. and S.P. developed the analytical concept that relates spectroscopic data to macroscopic solution parameters. M.H. provided the funding. C.Y.M., G.S., S.P., and M.H. wrote the draft manuscript and its revised versions.

References

[1] Gouaux, E., MacKinnon, R.: Principles of selective ion transport in channels and pumps. Science **310**(5753), 1461–1465 (2005)

[2] DuChanois, R.M., Porter, C.J., Violet, C., Verduzco, R., Elimelech, M.: Membrane materials for selective ion separations at the water–energy nexus. Advanced Materials **33**(38), 2101312 (2021) https://doi.org/10.1002/adma.202101312 https://advanced.onlinelibrary.wiley.com/doi/pdf/10.1002/adma.202101312

[3] Ershov, A., Xu, H., Li, Y., Tong, T., Epsztein, R.: Role of ion dehydration in ion-ion selectivity of dense membranes. Environmental Science & Technology **59**(34), 17997–18009 (2025) https://doi.org/10.1021/acs.est.5c04303 https://doi.org/10.1021/acs.est.5c04303. PMID: 40830835

[4] Deng, J., Xue, G., Li, C., Zhao, S., Zheng, Y., He, Y., Yuan, R., Wang, K., Mo, T., Xiang, Y., Chen, Y., Geng, Y., Wang, L., Feng, G., Hou, X., Li, M.: Accelerating ion desolvation via bioinspired ion channel design in nonconcentrated aqueous electrolytes. Journal of the American Chemical Society **147**(7), 5943–5954 (2025) https://doi.org/10.1021/jacs.4c15443 https://doi.org/10.1021/jacs.4c15443. PMID: 39907055

[5] Suo, L., Borodin, O., Gao, T., Olguin, M., Ho, J., Fan, X., Luo, C., Wang,

C., Xu, K.: “water-in-salt” electrolyte enables high-voltage aqueous lithium-ion chemistries. Science **350**(6263), 938–943 (2015) https://doi.org/10.1126/science.aab1595 https://www.science.org/doi/pdf/10.1126/science.aab1595

[6] Chen, L., Cao, L., Ji, X., Hou, S., Li, Q., Chen, J., Yang, C., Eidson, N., Wang, C.: Enabling safe aqueous lithium ion open batteries by suppressing oxygen reduction reaction. Nature Communications **11**(1), 2638 (2020) https://doi.org/10.1038/s41467-020-16460-w

[7] Jaumaux, P., Yang, X., Zhang, B., Safaei, J., Tang, X., Zhou, D., Wang, C., Wang, G.: Localized water-in-salt electrolyte for aqueous lithium-ion batteries. Angewandte Chemie International Edition **60**(36), 19965–19973 (2021) https://doi.org/10.1002/anie.202107389 https://onlinelibrary.wiley.com/doi/pdf/10.1002/anie.202107389

[8] Ahn, H., Kim, D., Lee, M., Nam, K.W.: Challenges and possibilities for aqueous battery systems. Communications Materials **4**(1), 37 (2023) https://doi.org/10.1038/s43246-023-00367-2

[9] Xia, M., Zhou, J., Lu, B.: Comprehensive insights into aqueous potassium-ion batteries. Advanced Energy Materials **15**(12), 2404032 (2025)

[10] Tang, X., Zhou, D., Zhang, B., Wang, S., Li, P., Liu, H., Guo, X., Jaumaux, P., Gao, X., Fu, Y., Wang, C., Wang, C., Wang, G.: A universal strategy towards high–energy aqueous multivalent–ion batteries. Nature Communications **12**(1), 2857 (2021) https://doi.org/10.1038/s41467-021-23209-6

[11] Ko, S., Nishimura, S.-i., Takenaka, N., Kitada, A., Yamada, A.: Practical issues toward high-voltage aqueous rechargeable batteries. Chem. Soc. Rev. **54**, 4200–4313 (2025) https://doi.org/10.1039/D4CS00779D

[12] Mahmood, A., Bai, Z., Wang, T., Lei, Y., Wang, S., Sun, B., Khan, H., Khan, K., Sun, K., Wang, G.: Enabling high-performance multivalent metal-ion batteries: current advances and future prospects. Chem. Soc. Rev. **54**, 2369–2435 (2025) https://doi.org/10.1039/D4CS00929K

[13] Hofmeister, F.: On the understanding of the effects of salts. Arch. Exp. Pathol. Pharmakol.(Leipzig) **24**, 247–260 (1888)

[14] Chi, E.Y., Krishnan, S., Randolph, T.W., Carpenter, J.F.: Physical stability of proteins in aqueous solution: Mechanism and driving forces in nonnative protein aggregation. Pharmaceutical Research **20**(9), 1325–1336 (2003) https://doi.org/10.1023/A:1025771421906

[15] Dumetz, A.C., Chockla, A.M., Kaler, E.W., Lenhoff, A.M.: Protein phase behavior in aqueous solutions: crystallization, liquid-liquid phase separation, gels, and aggregates. Biophysical journal **94**(2), 570–583 (2008)

[16] Flór, M., Vorobev, V., Mandalaparthy, V., Vegt, N.F.A., Cremer, P.S., Roke, S.: Unraveling the molecular pathways for structure "making"and "breaking"by ions in water. Journal of the American Chemical Society (2025) https://doi.org/10.1021/jacs.5c10984

[17] Figiel, P., Yu, G., Held, C.: Predicting thermodynamic properties of ions in single solvents and in mixed solvents using a modified born term within the epc-saft framework. Industrial & Engineering Chemistry Research **64**(18), 9406–9418 (2025) https://doi.org/10.1021/acs.iecr.5c00475 https://doi.org/10.1021/acs.iecr.5c00475

[18] Coupette, F., Lee, A.A., Härtel, A.: Screening lengths in ionic fluids. Phys. Rev. Lett. **121**, 075501 (2018) https://doi.org/10.1103/PhysRevLett.121.075501

[19] Coles, S.W., Park, C., Nikam, R., Kanduč, M., Dzubiella, J., Rotenberg, B.: Correlation length in concentrated electrolytes: Insights from all-atom molecular dynamics simulations. The Journal of Physical Chemistry B **124**(9), 1778–1786 (2020) https://doi.org/10.1021/acs.jpcb.9b10542 https://doi.org/10.1021/acs.jpcb.9b10542. PMID: 32031810

[20] Kim, P., Kang, R., Carter-Fenk, K., Wilson, K.R., Head-Gordon, M., Ahmed, M.: Structural evidence of interanionic hydrogen bonding in phosphoric acid solutions. Journal of the American Chemical Society **0**(0), (0) https://doi.org/10.1021/jacs.5c12699 https://doi.org/10.1021/jacs.5c12699. PMID: 41284755

[21] Dinpajooh, M., Biasin, E., Nienhuis, E.T., Mergelsberg, S.T., Benmore, C.J., Schenter, G.K., Fulton, J.L., Kathmann, S.M., Mundy, C.J.: Detecting underscreening and generalized kirkwood transitions in aqueous electrolytes. The Journal of Chemical Physics **161**(15), 151102 (2024) https://doi.org/10.1063/5.0234518 https://pubs.aip.org/aip/jcp/article-pdf/doi/10.1063/5.0234518/20215944/151102_1_5.0234518.pdf

[22] Dinpajooh, M., Intan, N.N., Duignan, T.T., Biasin, E., Fulton, J.L., Kathmann, S.M., Schenter, G.K., Mundy, C.J.: Beyond the debye–hückel limit: Toward a general theory for concentrated electrolytes. The Journal of Chemical Physics **161**(23), 230901 (2024) https://doi.org/10.1063/5.0238708 https://pubs.aip.org/aip/jcp/article-pdf/doi/10.1063/5.0238708/20300216/230901_1_5.0238708.pdf

[23] Böhm, F., Schwaab, G., Havenith, M.: Mapping hydration water around alcohol chains by thz calorimetry. Angewandte Chemie International Edition **56**(33), 9981–9985 (2017)

[24] Conti Nibali, V., Pezzotti, S., Sebastiani, F., Galimberti, D., Schwaab, G., Heyden, M., Gaigeot, M.-P., Havenith, M.: Wrapping up hydrophobic hydration: locality matters. The journal of physical chemistry letters **11**(12), 4809–4816 (2020)

[25] Pezzotti, S., Sebastiani, F., Dam, E.P., Ramos, S., Conti Nibali, V., Schwaab, G., Havenith, M.: Spectroscopic fingerprints of cavity formation and solute insertion as a measure of hydration entropic loss and enthalpic gain. Angewandte Chemie International Edition **61**(29), 202203893 (2022) https://doi.org/10.1002/anie.202203893 https://onlinelibrary.wiley.com/doi/pdf/10.1002/anie.202203893

[26] Bag, S., Pezzotti, S., Das Mahanta, D., Schulke, S., Schwaab, G., Havenith, M.: From local hydration motifs in aqueous acetic acid solutions to macroscopic mixing thermodynamics: A quantitative connection from thz-calorimetry. The Journal of Physical Chemistry B **127**(42), 9204–9210 (2023)

[27] Mahanta, D.D., Brown, D.R., Pezzotti, S., Han, S., Schwaab, G., Shell, M.S., Havenith, M.: Local solvation structures govern the mixing thermodynamics of glycerol–water solutions. Chemical Science **14**(26), 7381–7392 (2023)

[28] Mahanta, D.D., Brown, D.R., Webber, T., Pezzotti, S., Schwaab, G., Han, S., Shell, M.S., Havenith, M.: Bridging the gap in cryopreservation mechanism: Unraveling the interplay between structure, dynamics, and thermodynamics in cryoprotectant aqueous solutions. The Journal of Physical Chemistry B **128**(15), 3720–3731 (2024)

[29] Pezzotti, S., König, B., Ramos, S., Schwaab, G., Havenith, M.: Liquid–liquid phase separation? ask the water! The Journal of Physical Chemistry Letters **14**(6), 1556–1563 (2023)

[30] Pezzotti, S., Chen, W., Novelli, F., Yu, X., Hoberg, C., Havenith, M.: Terahertz calorimetry spotlights the role of water in biological processes. Nature Reviews Chemistry, 1–14 (2025)

[31] Schwaab, G., Sebastiani, F., Havenith, M.: Ion hydration and ion pairing as probed by THz spectroscopy. Angewandte Chemie International Edition **58**(10), 3000–3013 (2019)

[32] Schwaab, G., Pezzotti, S.: A new perspective on aqueous electrolyte solutions. Phys. Chem. Chem. Phys. **27**, 17585–17597 (2025) https://doi.org/10.1039/D5CP01781E

[33] Funke, S., Sebastiani, F., Schwaab, G., Havenith, M.: Spectroscopic fingerprints in the low frequency spectrum of ice (ih), clathrate hydrates, supercooled water, and hydrophobic hydration reveal similarities in the hydrogen bond network motifs. The Journal of Chemical Physics **150**(22), 224505 (2019) https://doi.org/10.1063/1.5097218

[34] Heyden, M., Sun, J., Funkner, S., Mathias, G., Forbert, H., Havenith, M., Marx, D.: Dissecting the thz spectrum of liquid water from first principles via correlations in time and space. Proceedings of the National Academy of Sciences **107**(27), 12068 (2010)

[35] Marcus, Y.: Ion Properties. Marcel Dekker Inc., New York, Basel (1997)

[36] Funkner, S., Niehues, G., Schmidt, D.a., Heyden, M., Schwaab, G., Callahan, K.M., Tobias, D.J., Havenith, M.: Watching the low-frequency motions in aqueous salt solutions: the terahertz vibrational signatures of hydrated ions. J. Am. Chem. Soc. **134**(2), 1030–5 (2012) https://doi.org/10.1021/ja207929u

[37] Śmiechowski, M., Forbert, H., Marx, D.: Spatial decomposition and assignment

of infrared spectra of simple ions in water from mid-infrared to thz frequencies: Li+ (aq) and f-(aq). The Journal of Chemical Physics **139**(1) (2013)

[38] Lobo, V., Quaresma, J.: Handbook of electrolyte solutions (Physical sciences data, vol. 41): Elsevier, Amsterdam, 1989 (ISBN 0-444-988847-5). xii+ 1168 pp.(Part A), xii+ 1186 pp.(Part B). Price Dfl. 1400.00. Elsevier (1990)

[39] Millero, F.J.: Molal volumes of electrolytes. Chemical Reviews **71**(2), 147–176 (1971)

[40] Jones, G., Ray, W.A.: The surface tension of solutions of electrolytes as a function of the concentration. i. a differential method for measuring relative surface tension. Journal of the American Chemical Society **59**(1), 187–198 (1937)

[41] Conde, M.R.: Properties of aqueous solutions of lithium and calcium chlorides: formulations for use in air conditioning equipment design. International Journal of Thermal Sciences **43**(4), 367–382 (2004)

[42] Zelsmann, H.R.: Temperature dependence of the optical constants for liquid h2o and d2o in the far ir region. Journal of Molecular Structure **350**(2), 95–114 (1995) https://doi.org/10.1016/0022-2860(94)08471-S

[43] Bertie, J., Lan, Z.: Infrared Intensities of Liquids XX: The Intensity of the OH Stretching Band of Liquid Water Revisite, and the Best Current Values of the Optical Constants of H20(l) at 25 °C between 15,000 and 1 cm^{-1}. Appl. Spectrosc. **50**(8), 1047–1057 (1996)

[44] Ellison, W.: Permittivity of pure water, at standard atmospheric pressure, over the frequency range 0–25 thz and the temperature range 0–100 c. J. Phys. Chem. Ref. Data **36**(1), 1–18 (2007)

[45] Lunkenheimer, P., Emmert, S., Gulich, R., Köhler, M., Wolf, M., Schwab, M., Loidl, A.: Electromagnetic-radiation absorption by water. Physical Review E **96**(6), 062607 (2017)

[46] Stokes, R.: Thermodynamics of Solutions vol. 2, pp. 1–28. CRC Press, Boca Raton (2018). Chap. 1

[47] Press, W., Flannery, B.P., Teukolsky, S., Vetterling, W.T.: Numerical Recipes: The Art of Scientific Computing. Cambridge University Press, Cambridge (1986)

[48] Remsing, R.C., Weeks, J.D.: Role of local response in ion solvation: Born theory and beyond. The Journal of Physical Chemistry B **120**(26), 6238–6249 (2016) https://doi.org/10.1021/acs.jpcb.6b02238 https://doi.org/10.1021/acs.jpcb.6b02238. PMID: 27183036

Extended Data

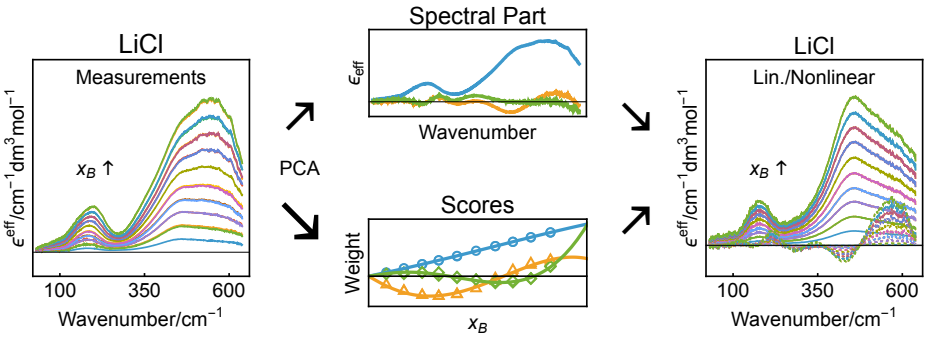


Fig. 5 General principle of PCA with LiCl as an example. The concentration-dependent measurements (left) are split into their relevant spectroscopic components (center, top) and their scores as a function of mol fraction (center, bottom) using PCA. The scores are fitted as a superposition of a linear term and a set of nonlinear functions derived from a multipole-expansion model for the solute and solvent activity coefficients. This allows us to separate the measured spectra into their linear (full lines) and nonlinear (dashed) contributions as a function of mol fraction (right)

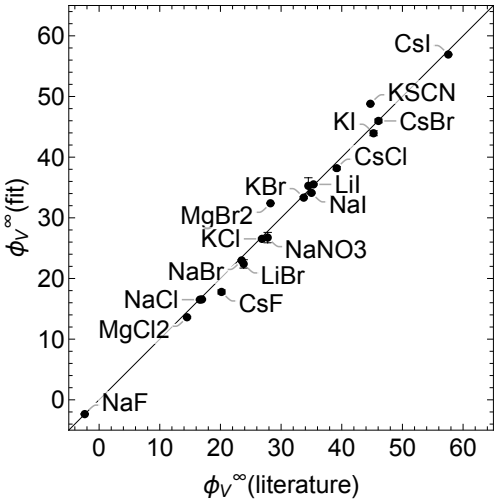


Fig. 6 Comparison of the apparent molar volumes at infinite dilution from the activity-based fit in this work and literature data.[35]

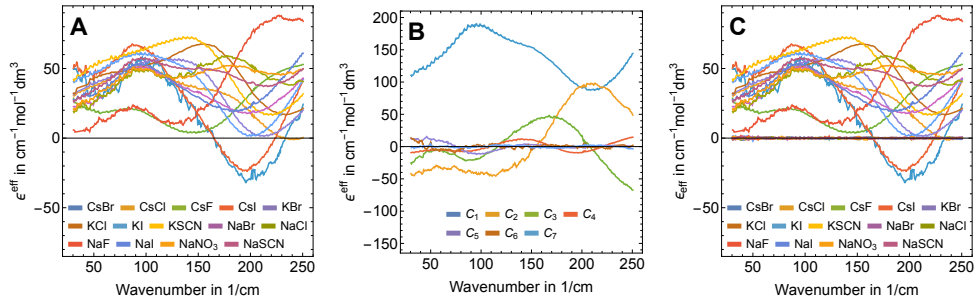


Fig. 7 PCA of the low frequency range (30-250 cm^{-1}) of the linear spectroscopic components of 14 electrolytes. For the analysis, Li and Mg salts were excluded due to their strong ionic rattling modes. A: Original spectra; B: The major seven principal components; C: Reconstructed spectra and residuals when using the first seven principal components.

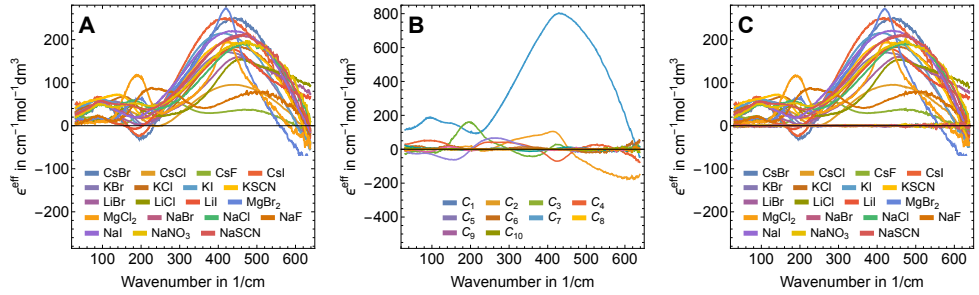


Fig. 8 PCA of the full frequency range (30-640 cm^{-1}) of the linear spectroscopic components of 19 electrolytes, including Li and Mg salts. A: Original spectra; B: The first ten principal components; C: Reconstructed spectra and residuals when using the first ten principal components.

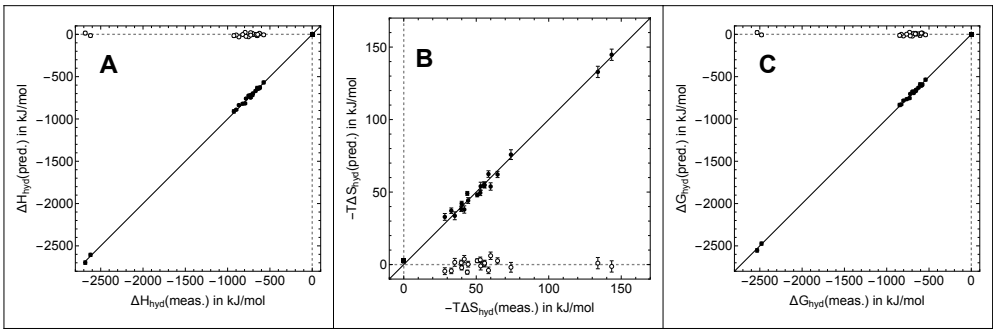


Fig. 9 Comparison between measured and predicted absolute hydration energies. A: Hydration enthalpy; B: Hydration entropy ($-T\Delta S_{\mathrm{hyd}}$); C: Hydration Gibbs free energy. See text for model details.

Table 3 The four spectral weights (scores) of the 19 electrolytes that are relevant for the linear models of mixing energies and transport properties. The values for CsI have been fixed to ensure that C_1 corresponds to the CsI spectrum.

salt	$\tilde{s}_1$	$\tilde{s}_2$	$\tilde{s}_3$	$\tilde{s}_4$
CsBr	0.727	-0.141	0.032	0.201
CsCl	1.080	0.264	0.701	-0.593
CsF	0.649	0.487	-0.067	-0.110
CsI	1.000	0.000	0.000	0.000
KBr	1.208	0.250	0.719	0.398
KCl	1.520	0.566	1.122	0.341
KI	1.307	0.279	0.466	0.528
KSCN	1.677	0.513	1.051	0.553
LiBr	0.410	0.147	0.144	0.353
LiCl	0.718	0.521	0.610	0.305
LiI	0.329	0.104	-0.167	0.299
MgBr2	0.871	0.709	0.617	-0.398
MgCl2	1.207	1.182	1.304	-0.465
NaBr	1.089	0.406	0.398	0.314
NaCl	1.388	0.746	0.840	0.156
NaF	1.003	1.007	0.160	0.195
NaI	1.201	0.496	0.268	0.476
NaNO3	1.405	0.748	0.718	0.191
NaSCN	1.475	0.666	0.733	0.399

Supplementary Information

S1.1 Terms and Definitions

Table S1 Basic definitions and equations used in this work to describe electrolyte and water activities. Based on our recent work[32] and standard thermodynamic relationships.[46]

Function	Equation
Definitions	
Molar mass of water	$M_w = 18.015$ g/mol
moles water per 1 kg	$n_0 = \frac{1000g}{M_w} = 55.509$ moles
electrolyte molality	m_B mol/kg solvent
total amount of substance/kg solvent	$n = n_0 + m_B$ mol
electrolyte mol fraction	$x_B = \frac{m_B}{m_B+n_0}$
water mol fraction	$x_w = 1 - x_B = \frac{n_0}{m_B+n_0}$
one-molal reference solution	$m^0 = 1$ moles/kg solvent
Stoichiometric coefficients	
cation	ν_+
anion	ν_-
total	$\nu = \nu_+ + \nu_-$
Chemical potentials	
water activity	$\ln a_w = -\nu \frac{x_B}{x_w} \phi$
electrolyte activity coefficient	$\ln \gamma_\pm$
Osmotic coefficient	$\phi = 1 + \frac{1-x_B}{x_B} \int_0^{x_B} \frac{x}{1-x} d \ln \gamma_\pm$
Multipole parametrization	
electrolyte activity coefficient	$\ln \gamma_\pm = \sum_{l=1}^{\leq 3} \ln \gamma_\pm^{(l)}$
osmotic coefficient	$\phi = 1 + \sum_{l=1}^{\leq 3} \phi^{(l)}$
$\ln \gamma_\pm$ multipole term	$\ln \gamma_\pm^{(l)} = D_l \left(\frac{x_B}{x_h^l}\right)^{\lambda_l} \ln \left[\left(\frac{x_B}{x_h^l}\right)^{\lambda_l}\right]$
ϕ multipole term	$\phi^{(l)} = \frac{1-x_B}{x_B} \int_0^{x_B} \frac{x}{1-x} d \ln \gamma_\pm^{(l)}$
$\phi^{(l)}$ from [32]	$\phi^{(l)} = \frac{1-x_B}{x_B} D_l \frac{\lambda_l}{x_h^{\lambda_l}} \left[\left(1 + \lambda_l \ln \left[\frac{x_B}{x_h}\right]\right) B_{x_B}(1+\lambda_l, 0) - \lambda_l x_B^{1+\lambda_l} \Phi(x_B, 2, 1+\lambda_l)\right]$
$\phi^{(l)}$ alternative	$\phi^{(l)} = (1-x_B) D_l \lambda_l \left(\frac{x_B}{x_h}\right)^{\lambda_l} \times \left[\left(1 + \lambda_l \ln \left[\frac{x_B}{x_h}\right]\right) \Phi(x_B, 1, 1+\lambda_l) - \lambda_l \Phi(x_B, 2, 1+\lambda_l)\right]$
Lerch transcendent	$\Phi(x_B, 2, 1+\lambda_l) = \sum_{k=0}^{\infty} \frac{x_B^k}{(1+\lambda_l+k)^2}$
	$\Phi(x_B, 1, 1+\lambda_l) = \sum_{k=0}^{\infty} \frac{x_B^k}{(1+\lambda_l+k)}$
Incomplete Euler Beta	$B_{x_B}(1+\lambda_l, 0) = \int_0^{x_B} \frac{t^{\lambda_l}}{(1-t)} dt$
Fit parameters	
Interaction strength	D_l ($l = 1$: dipole, $l = 2$: quadrupole, $l = 3$: octupole)
Interaction exponent	λ_l
Crossover mol fraction	x_h^l, $0 < x_h^1 \leq 1$, $x_h^2 = x_h^3 = 1$

S1.2 Concentration Dependent Measurements

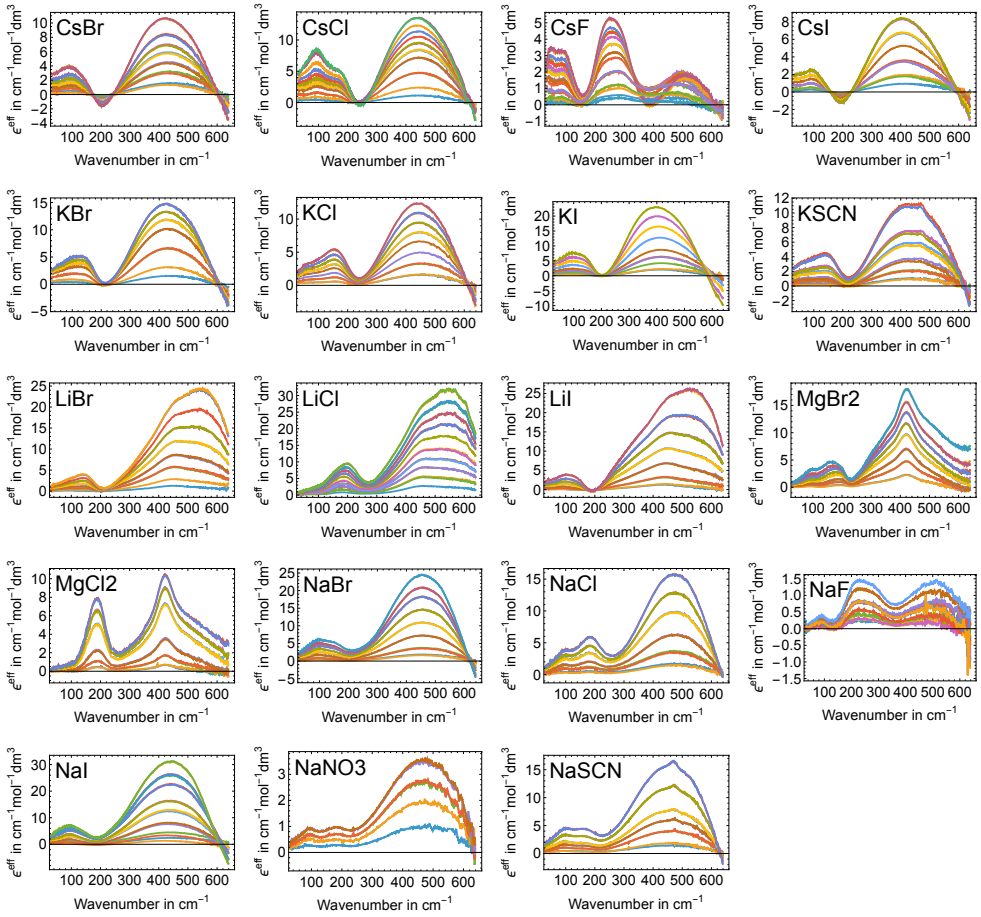


Fig. S1 Effective molar extinction coefficients of 19 electrolytes as a function of concentration.

S1.3 Connecting the Multipole Model and Volume Properties

S1.3.1 Global Fits of $\ln \gamma_{\pm}$ and the Osmotic Coefficient, ϕ

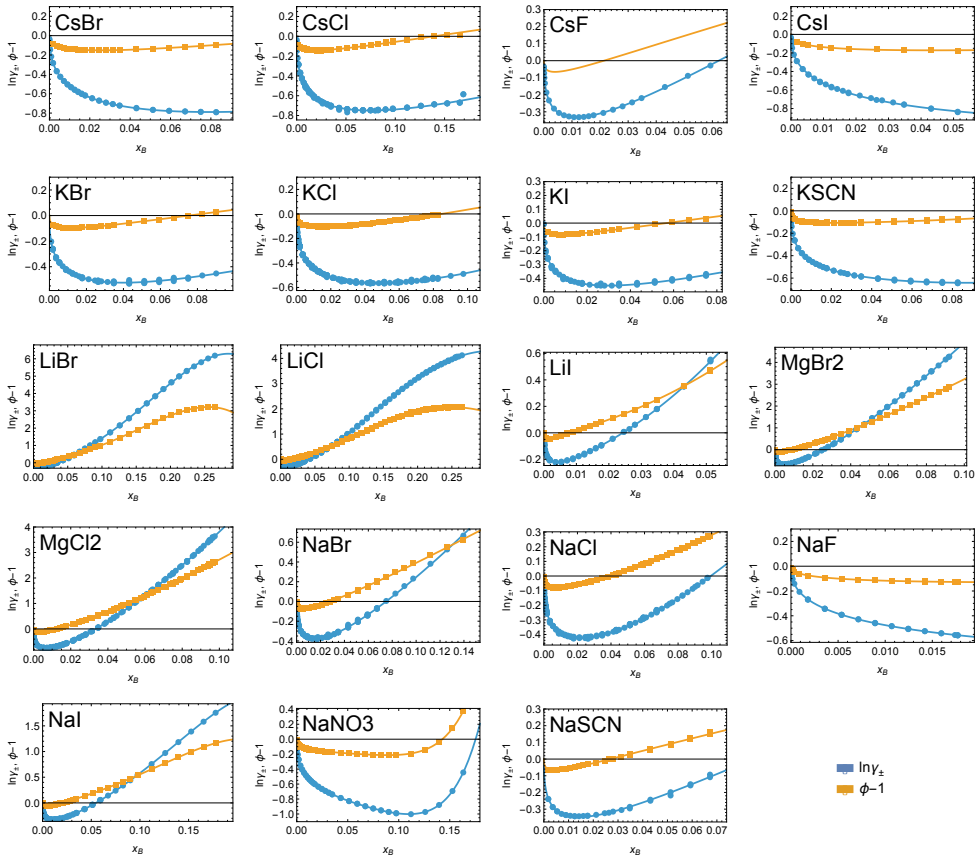


Fig. S2 Fit of the activity and osmotic coefficients for 19 electrolytes.

S1.3.2 Effective Molar Volumes as Derived from the Activity-Coefficient Model

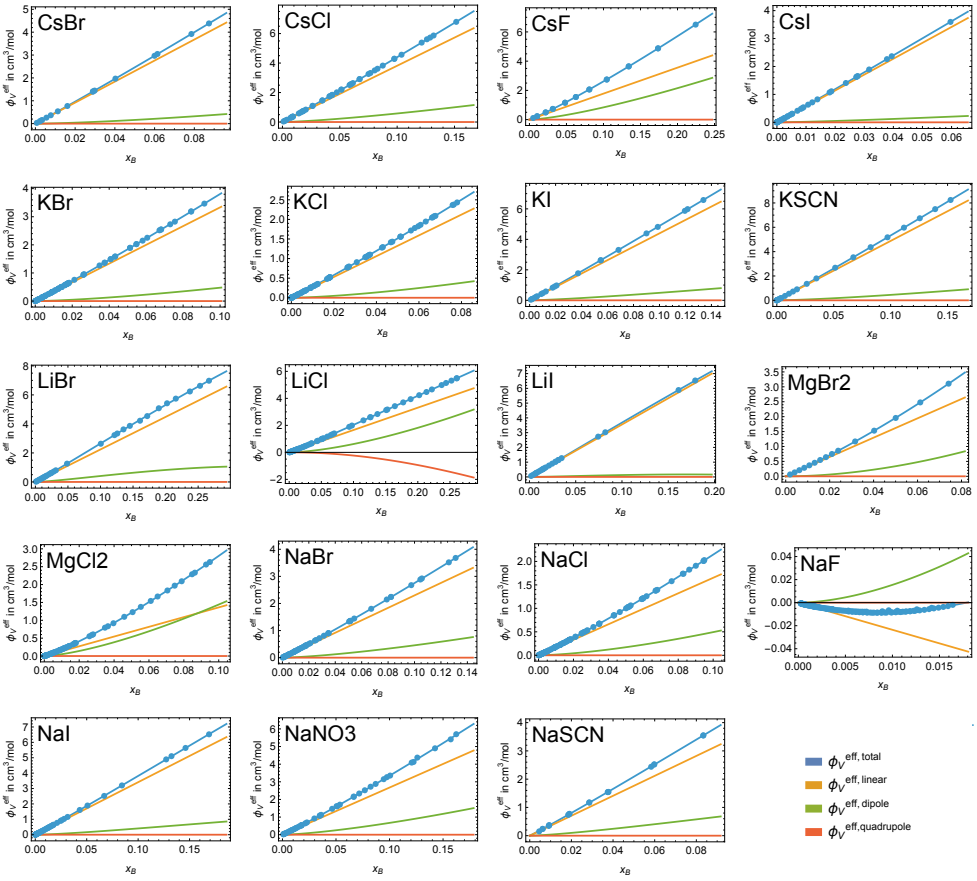


Fig. S3 Fit of the excess molar volume as a function of electrolyte mol fraction for 19 electrolytes. The linear and nonlinear components (for individual multipole expansion terms) are also shown. LiCl is the only electrolyte that shows a quadrupolar contribution.

S1.3.3 Densities as Derived from the Activity-Coefficient Model

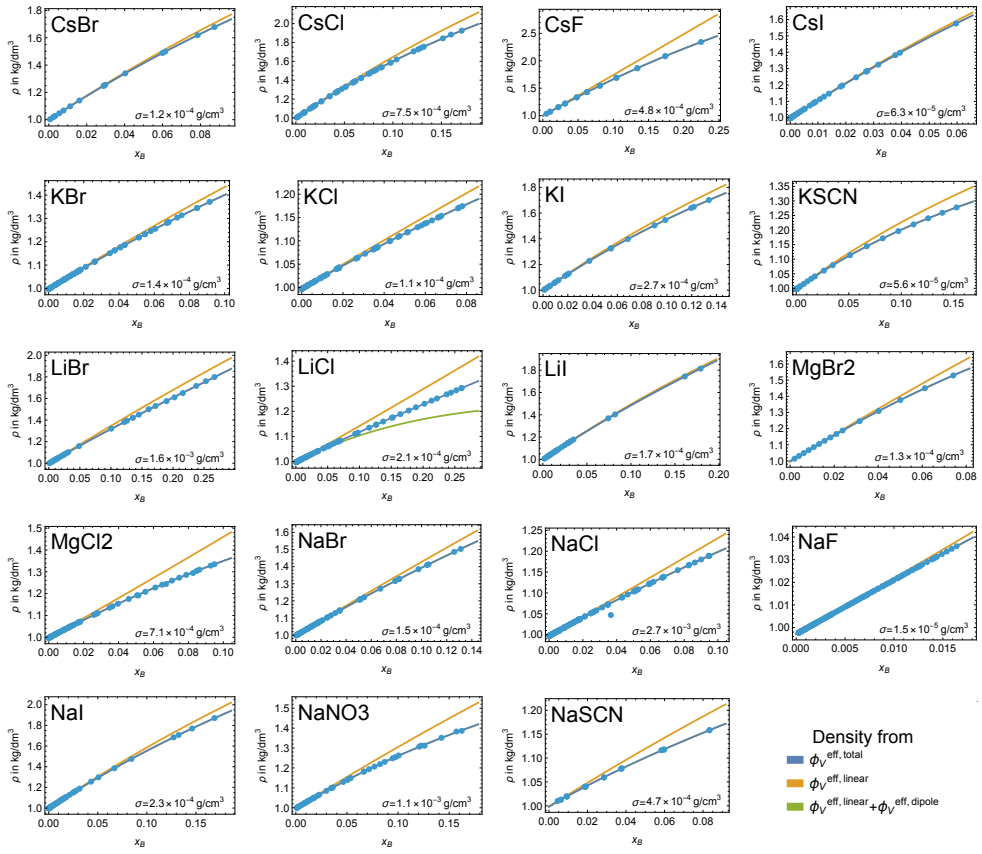


Fig. S4 Fit of the excess density as a function of electrolyte mol fraction for 19 electrolytes. The linear and nonlinear components (by multipole expansion term) are also shown. LiCl is the only electrolyte that shows a significant quadrupolar contribution.

S1.4 Principal Component Analysis of Concentration-Dependent Molar Extinction Coefficients

S1.4.1 Relevant Principal Components

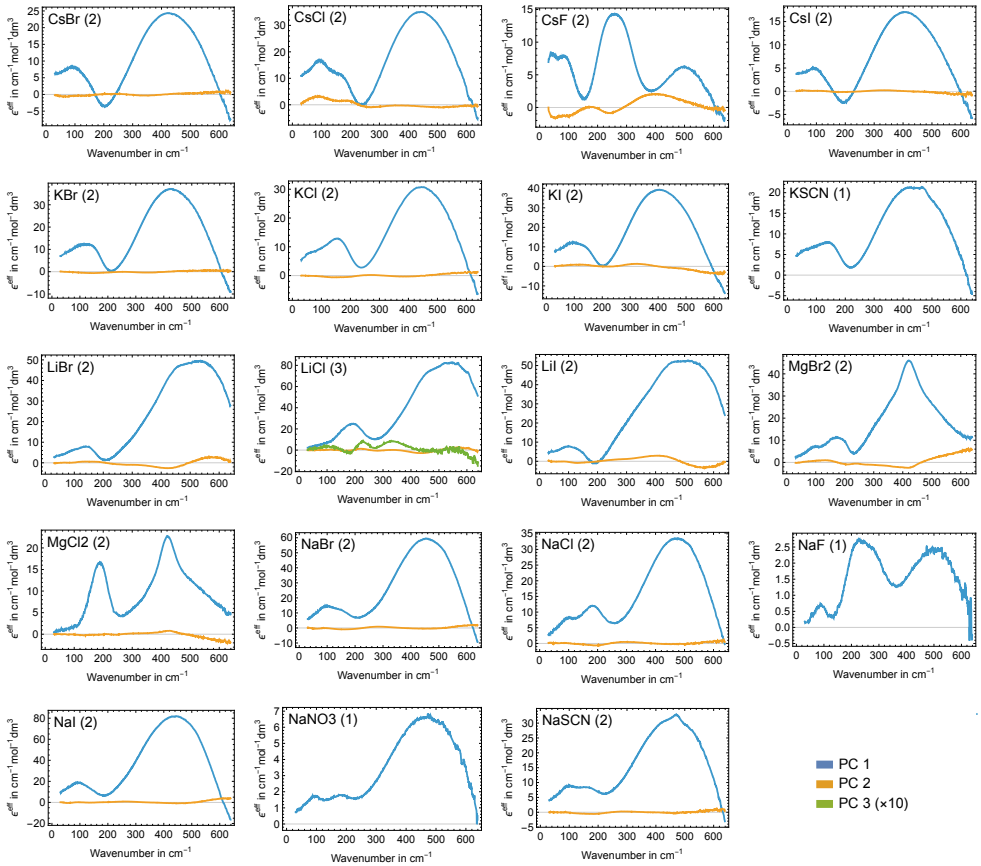


Fig. S5 Relevant principal components for 19 electrolytes. The number in brackets indicates the number of components necessary to describe the spectroscopic measurements within experimental error.

S1.4.2 Score Fits Using the Functions Derived from the Activity-Coefficient Model

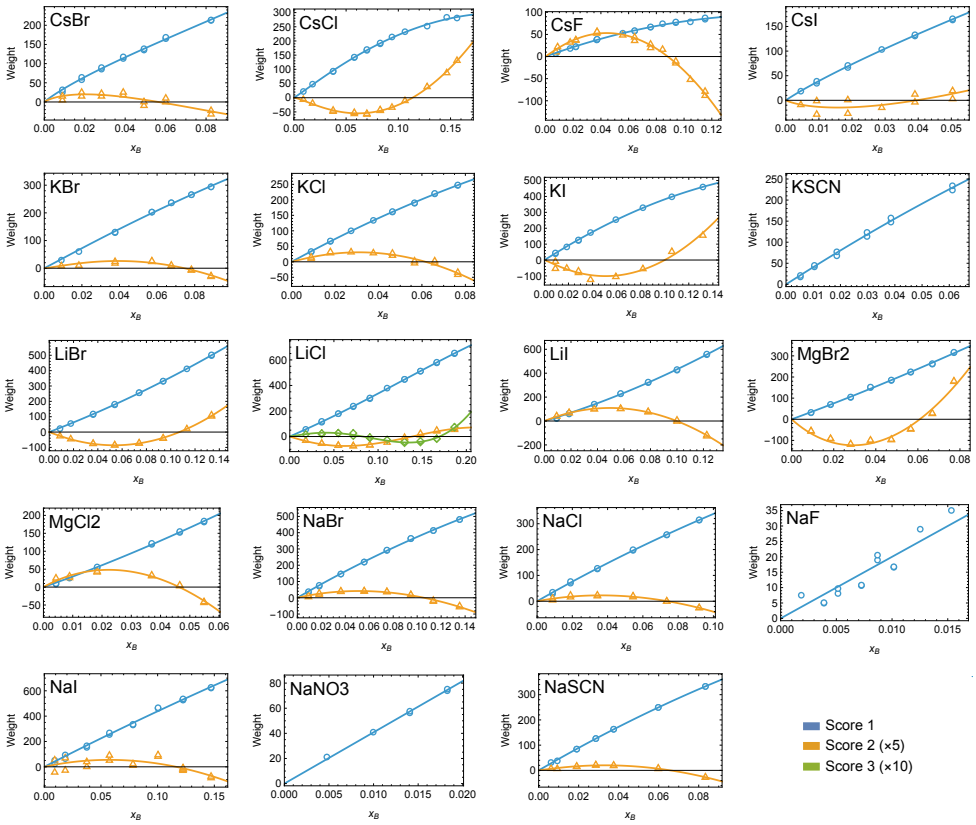


Fig. S6 Fit of the relevant scores for 19 electrolytes.

S1.4.3 Spectral Reconstruction from Relevant Principal Components and Score Fitfunctions

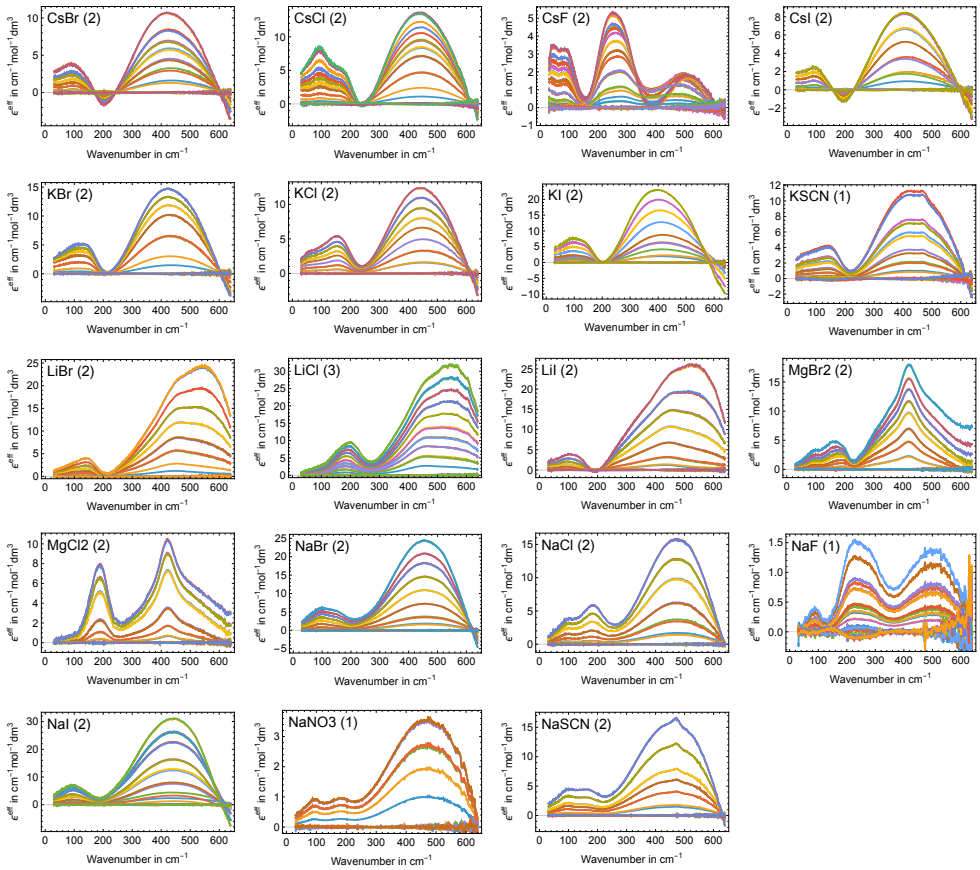


Fig. S7 Spectra reconstructed from the activity-based score fit and fit residuals for 19 electrolytes.

S1.5 Linear and Nonlinear Contributions to $\epsilon^{\mathbf{eff}}$

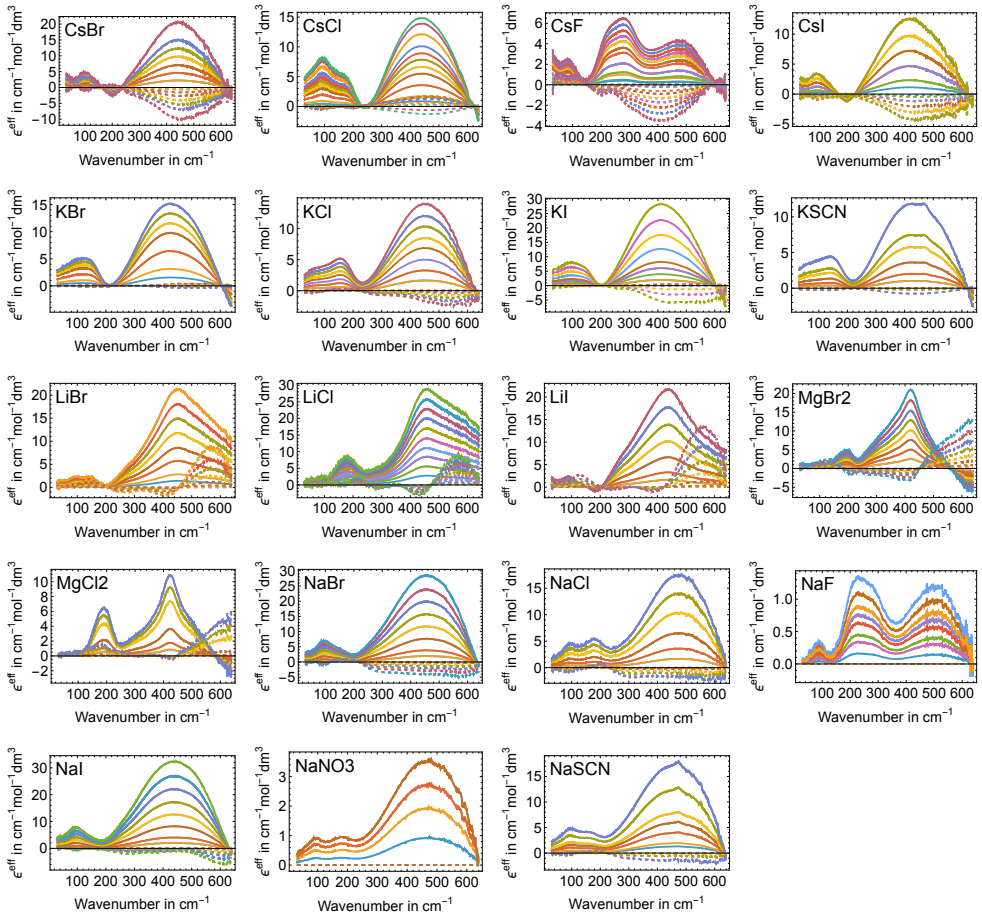


Fig. S8 Linear and nonlinear contributions to the observed molar extinction coefficients for 19 electrolytes. The cation dominates the shape of the nonlinear contribution.

S1.6 Dissection of Linear Spectra into H-bond related and Ion-Specific Contributions

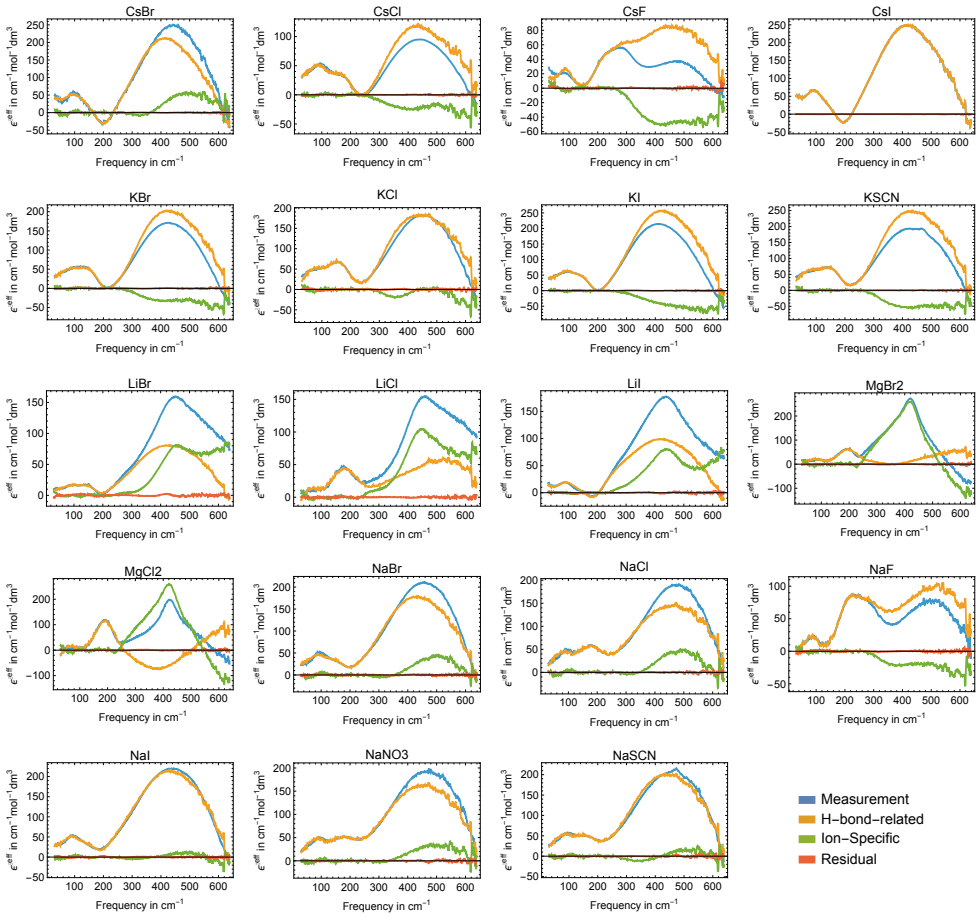


Fig. S9 Separation of linear spectra (blue) into their H-bond-related (yellow) and ion-specific (green) spectroscopic contributions. The residual after applying a ten-component PCA is shown in red.